INSTITUTO
UNIVERSITÁRIO
DE LISBOA

Fully Automatic Assessment for Left Ventricle Image Segmentation and Feature Extraction

António Maria Sousa Gomes Neto

Master's in Computer Science and Business Management,

Supervisor:
PhD João Pedro Oliveira,
Assistant Professor,
ISCTE-IUL

Co-supervisor:
PhD Luís Afonso Brás Simões do Rosário,
Invited Assistant Professor,
Faculdade de Medicina da Universidade de Lisboa

October, 2023

TECNOLOGIAS
E ARQUITETURA

Department of Information Science and Technology

Fully Automatic Assessment for Left Ventricle Image Segmentation and Feature Extraction

António Maria Sousa Gomes Neto

Master's in Computer Science and Business Management,

Supervisor:
PhD João Pedro Oliveira,
Assistant Professor,
ISCTE-IUL

Co-supervisor:
PhD Luís Afonso Brás Simões do Rosário,
Invited Assistant Professor,
Faculdade de Medicina da Universidade de Lisboa

October, 2023

Acknowledgements

I would like to start by thanking my supervisors, Professor João Pedro Oliveira, Professor Luis Rosário, as well as Professor Mauricio Breternitz for their amazing efforts in this three-year journey. It wasn't easy to get here, but I'm forever thankful for their dedication to my thesis as well as their relevant work that goes beyond it in this very important area of science.

I would like to extend my gratitude to Instituto de Telecomunicações (IT), for their support and providing computacional and infrastructural conditions for the development of this thesis. As well as to Affidea Caselas, for opening their doors and providing valuable data, that enriched the depth and scope of this work.

Also a special thank you to João Silva, my partner in crime, who was with me every step of the way in this endeavor.

To António Lorvão for his unwavering support.

To Neuza who always encouraged me to keep going.

Finally, to my Family and Friends for their unconditional love and support throughout this period.

I've been at ISCTE for 7 years now, and however contradictory, I'm happy to say I feel sad to leave.

Resumo

A segmentação e medições do ventrículo esquerdo, assim como do miocárdio, são práticas clínicas comuns no diagnóstico de doenças associadas ao ventrículo esquerdo. A técnica de ressonância magnética é vastamente reconhecida como uma referência para a avaliação não invasiva da função do ventrículo esquerdo. Na última década muitos estudos foram desenvolvidos com o objetivo de melhorar técnicas de segmentação e classificação automáticas, em vários datasets de ressonância cardíaca.

Contudo, a maioria dos métodos propostos não produz justificações nem dados clinicamente relevantes que suportem o diagnóstico. Para colmatar esta falha, nesta dissertação, propomos um pipeline automático para a segmentação do ventrículo esquerdo, assim como a avaliação da sua função. O pipeline proposto tem por base um método de segmentação, estado da arte (nnU-Net), cujo resultado é melhorado através da aplicação de dois active contours para delinear contornos mais suaves e robustos. Posteriormente, métodos automáticos de extração de medidas foram propostos para a identificação de características locais e globais das estruturas segmentadas.

Os resultados obtidos mostram que o método proposto para otimização da segmentação mantém a precisão, enquanto permite uma melhor extração de características do ventrículo, produzindo uma segmentação mais robusta. Além do mais, o método de extração de características proposto provou-se eficaz na produção de dados clinicamente relevantes para a avaliação da função do ventrículo esquerdo.

Keywords: Deep Learning, Machine Learning, Ventrículo Esquerdo, Segmentação de Imagem Médica, Extração de Características, Ressonância Magnética.

Abstract

The segmentation and measurement of the left ventricle (LV) and the myocardium (MYO) are common clinical practices in the diagnosis of left ventricular conditions. Magnetic resonance (MRI) is recognized as a reference for non-invasive assessment of left ventricular function. Many studies over the last decades have focused on improving automatic segmentation and classification approaches, with multiple datasets for cardiac MRI. However, most automatic methods fail to provide reasoning and clinically relevant data to support the diagnosis. In this dissertation, we propose a novel fully automatic pipeline for left-ventricular segmentation and function assessment. The proposed pipeline leverages a state-of-the-art segmentation method (nnU-Net), which is then enhanced through the application of two active contours for smoother and more robust contour delineation. Automatic feature extraction methods are then proposed for the assessment of both local and global features within cardiac structures. Results show that the presented segmentation enhancements approach maintains accuracy while improving feature-extraction capabilities and robustness. Furthermore, the proposed feature extraction methods proved effective in providing clinically relevant data for assessing left ventricular function.

Keywords: Deep Learning, Machine Learning, Left Ventricle, Medical Image Segmentation, Feature Extraction, Cardiac MRI.

Contents

Acronyms

ACDC: Automatic Cardiac Diagnosis Challenge
AHA: American Heart Association
APD: Average Perpendicular Distance
ARV: Abnormal Right Ventricle

CD: Center Distance
CE mark: Conformité Européenne mark
CMR: Cardiac MRI
CNN: Convolutional Neural Network
CRISP-DM: Cross-Industry Standard Process for Data Mining
CT: Computerized Tomography

DCM: Dilated Cardiomyopathy
DICOM: Digital Imaging and Communications in Medicine

ED: End of Diastole
EF: Ejection Fraction
ES: End of Systole

FCN: Fully Convolutional Neural Network
FDA: Food and Drug Administration

HCM: Hypertrophic Cardiomyopathy

ISO: International Organization for Standardization

LV: Left Ventricle
LVMT: Left Ventricular Myocardial Thickness

MINF: Previous Myocardial Infarction
MRF: Markov Random Fields
MRI: Magnetic Resonance Imaging
MYO: Myocardium

NIFTI: Neuroimaging Informatics Technology Initiative
NOR: Healthy/Normal subjects

PDE: Partial Differential Equation

RNN: Recurrent Neural Network
ROI: Region of Interest
RQ1: Research Question 1
RQ2: Research Question 2
RQ3: Research Question 3
RV: Right Ventricle

SD: Standard Deviation
SV: Stroke Volume

List of Figures

List of Tables

CHAPTER 1

Introduction

1.1. Motivation and Context

Each year cardiovascular diseases are responsible for an estimated 17.9 million deaths and are amongst the leading causes of death worldwide [**1**]. As a way of preventing and detecting these pathologies medical exams like echography, magnetic resonance imaging (MRI), and computerized tomography (CT) among others are highly used. MRI is recognized as a reference modality for the non-invasive assessment of left ventricular function supplying information on muscle perfusion, tissue viability, blood flow, and morphology [**2**]. Through Cardiac MRI we can assess the left and right ventricular ejection fractions (EF) and stroke volumes (SV), the left ventricle mass, and the myocardium thickness. However, this requires an accurate segmentation of the left (LV) and right (RV) ventricles.

Segmenting cardiac structures manually is a long process, therefore, as there is not yet commercial software with fully automatic segmentation methods, clinicians rely on semi-automatic approaches where the user defines the region of interest (ROI). The segmentation process will also need to be tuned by the user in this type of software. These approaches are time-consuming and prone to intra and inter-observer variability.

Several international challenges have taken place in an attempt to improve the state-of-the-art of automatic cardiac segmentation. While some great improvements were achieved until 2012 in 4 challenges [**3, 4, 5, 6**], none had yet proposed deep learning methods. In 2017 a new challenge and dataset for automatic segmentation of LV, RV, and myocardium (MYO), and automatic pathology detection, was presented by Bernard et al. [**7**]. In this challenge, new deep learning approaches surpassed all prior methods and pushed the technology to a new standard.

Further investigations are still required before such software is approved by accreditation agencies (CE mark, FDA, ISO, etc.) and gets integrated into MRI consoles. Also, the field of explainability needs to be explored, as the diagnosis can only be fully accepted by the community if physiological reasons are provided to justify the classification attributed to "black box" methods. Deep learning methods are usually attributed to this denomination as the user is not aware of their learning process nor is it accessible. Although these studies compose a very bright picture of what is ahead in the field of medical image segmentation and classification, many pathologies are yet to be approached with these technologies.

In this work, we propose a novel fully automatic pipeline, enhancing current state-of-the-art segmentation and feature extraction approaches to provide relevant cardiac data for left-ventricular function assessment.

1.2. Problem Formulation

The heart comprises multiple complex structures each representing a separate problem for both segmentation and feature extraction. This dissertation focuses on left-ventricular segmentation and feature extraction in the automatic assessment of cardiac features. This section aims to provide more context to this problem from both an anatomical standpoint as well as to limitations of current approaches.

1.2.1. Anatomical Context

This subsection aims to make a brief introduction to the cardiac cycle and structure, providing context to coming references pertaining to specific events or structures.

Cardiac Chambers

The heart is composed of four chambers. The two superior chambers, responsible for receiving blood are the atria (entry chambers), while the two inferior pumping chambers, responsible for ejecting blood from the heart, are the ventricles [**8**]. Below we present a succinct description of each chamber as well as their role in the cardiac cycle:

- **Right Atrium:** The right atrium is on average 2 to 3 mm thick and is responsible for receiving deoxygenated blood from the veins and passing it through to the RV;
- **Left Atrium:** The left atrium is around the same size as the right atrium and is responsible for receiving oxygenated blood from the lungs and ejecting it into the LV;
- **Right Ventricle:** The RV is on average 4 to 5 mm thick and constitutes the majority of the heart's anterior surface. During the cardiac cycle, blood is ejected from the RV to the lungs;
- **Left Ventricle:** The LV is the thickest heart chamber, with an average thickness of 10 to 15 mm, and constitutes the apex of the heart. This chamber is responsible for irrigating the body through the aorta.

Layers of the Heart Wall

The heart wall is composed of three layers [**8**]:

- **Epicardium:** The epicardium is a thin and smooth protective layer, which is the lining of the wall;
- **Myocardium:** The MYO, a middle layer, is responsible for the heart's contractile functionality and is approximately 95% of the heart wall;
- **Endocardium:** The endocardium is the inner layer of the cardiac wall and lines the heart chambers and valves.

Cardiac Cycle

The cardiac cycle is composed of 2 phases, systole and diastole [**10, 11**]:

- **Diastole**: This stage starts with the closure of the aortic valve and concludes with the closure of the mitral valve. During diastole, both ventricles are in a

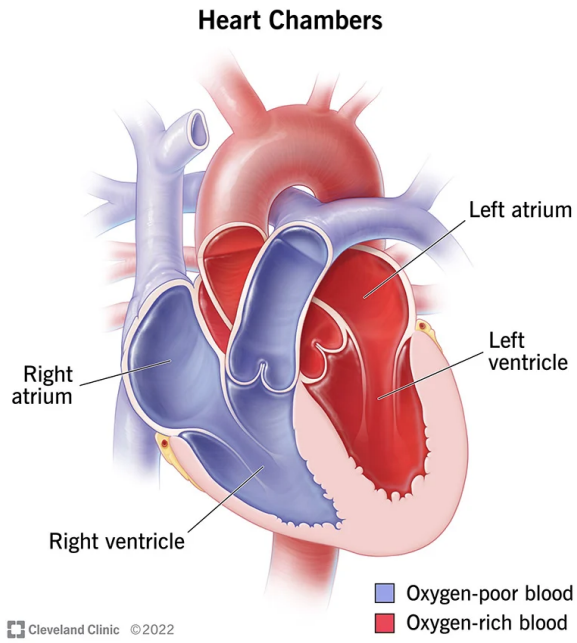

FIGURE 1.1. Heart chambers from [**9**].

relaxed state and are filled with blood. The end of the diastolic phase (ED) is when the heart achieves its maximum volume;

- **Systole**: This stage of the cardiac cycle in which there is ventricular contraction and ejection of blood to the valves. It begins when the mitral valve closes and ends with the closure of the aortic valve. The end of the systolic phase (ES) represents the moment when the contraction phase ends and is where the heart achieves its minimum volume.

Ventricular Slices

In the context of tomographic imaging of the heart the American Heart Association (AHA) [**12**] provides a standardized myocardial segmentation and nomenclature system. Here three main slices are described (Figure 1.2):

- **Basal**: The basal slice represents the region of the heart closest to the base or the top of the left ventricle, near the connection to the atria;
- **Mid**: The mid-slice, also known as the mid-cavity slice, refers to a section of the left ventricle that is located between the apex and the base of the heart, roughly in the middle of the ventricle;
- **Apical**: The apical slice corresponds to the apex or the tip of the left ventricle.

1.2.2. The Problem

The LV plays a critical role in providing oxygenated blood to the body and is therefore very relevant in cardiac function and health. Multiple conditions such as Dilated Cardiomyopathy (DCM) and Hypertrophic Cardiomyopathy (HCM) can be assessed through the evaluation of local and global features of the LV chamber.

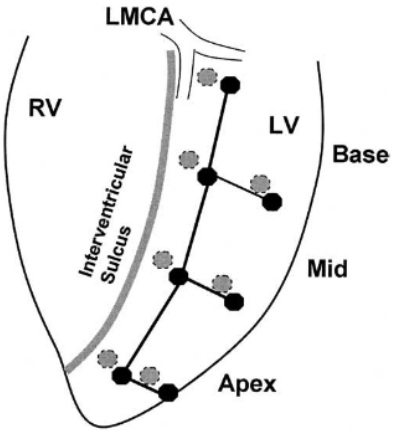

FIGURE 1.2. LV slice representation from [**13**].

Currently, practitioners rely mostly on semi-automatic tools for cardiac segmentation, therefore requiring manual input by a trained cardiologist. Current accomplishments in the area have focused on designing automatic highly accurate approaches to segment cardiac structures. However, most of these studies fail to propose automatic feature extraction methods for condition assessment. While some work has been done in the area of disease classification, these approaches fail to deliver automatic solutions that can aid in LV-related pathology identification while providing reliable reasoning and data to support the diagnosis.

1.3. Research Questions

This dissertation intends to propose an automatic segmentation and feature-extraction pipeline that provides clinically relevant data in the left-ventricular function assessment, by addressing the following research questions:

RQ1: Can current state-of-the-art segmentation methods be leveraged to build a reliable basis for left-ventricular function assessment?

RQ2: How can the robustness of existing state-of-the-art segmentation techniques be enhanced to enable more reliable and accurate feature extraction?

RQ3: Can fully automatic pipelines for feature extraction be developed and optimized to provide accurate and clinically relevant data for left-ventricular function assessment, without recurring to manual input?

1.4. Contributions

This work proposes multiple contributions to the field of cardiac image segmentation and feature extraction. In the scope of the work, multiple artifacts were proposed and implemented:

- **DICOM to NIFTI image converter**, capable of identifying multiple viewing planes and building 3D NIFTI representations of the DICOM files provided;

- **Enhanced Automatic Segmentation Model** that achieves a high level of accuracy and is enhanced for feature extraction;
- **Feature Extraction Module** that allows for global and local features to be extracted from the segmentation output;
- **Point Pairing Method** which allows the identification of segments of interest for local feature extraction.

All these contributions jointly define our proposed automatic pipeline capable of segmenting and providing regional and global features for LV function assessment.

1.5. Research Methodology

The chosen methodology for this work was the CRoss-Industry Standard Process for Data Mining (CRISP-DM). CRISP-DM [**14**] became widely known in the community as one of the most reliable process models for data science processes. It provides a structured and systematic approach to data analysis and modeling divided into 6 main phases (Figure 1.1). As a very versatile and flexible framework, below we provide context over each stage of this methodology, with emphasis on each's role within the thesis:

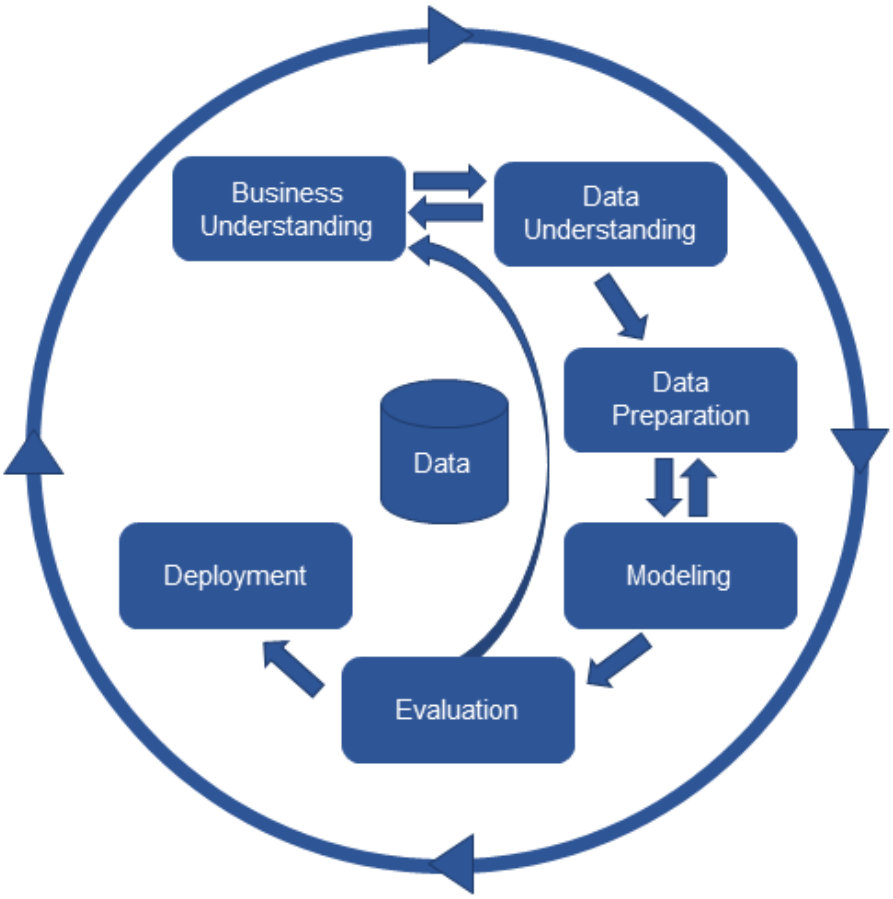

FIGURE 1.3. CRISP-DM (Chapman et al., 2000).

- **Business Understanding**: This initial phase is where we aim to understand what has already been done in the areas of study of this thesis, as well as the

relevancy of the work that will be executed. This stage is documented through the introduction and literature review chapters (chapters 1 and 2);

- **Data Understanding**: After having a well-defined structure for the proposed work, this stage focuses on analyzing the data that will be used in the scope of the thesis, assessing quality and relevance. This stage is documented in the third chapter, Data Understanding and Proposed Architecture (see section 3.1);
- **Data Preparation**: This stage aims to explore the data available and chosen for the work, and transform it to suit the needs of the subsequent modeling stage. This stage is documented in the segmentation chapter (see section 4.1);
- **Modeling**: In the modeling stage we establish the evaluation criteria, as well as execute an iterative process of fine-tuning the algorithm to achieve optimal results. This stage is documented in the enhanced boundary definition section as well as through the feature extraction chapter (section 4.2 and chapter 5);
- **Evaluation**: The evaluation stage consists of identifying through the established metrics to assess the effectiveness in addressing the business problems (in this case research questions). This stage is documented through the results sections of both chapters 4 and 5 (see sections 4.6 and 4.5);
- **Deployment**: For this thesis no deployment stage was executed, as the aim of the work is not to produce a production-ready solution.

1.6. Thesis Organization

This section provides an outline of this thesis structure, providing context for each chapter's role within the document:

(1) **Introduction:** In the opening chapter we provide the context and motivation behind the thesis, defining research questions and research methodology.

(2) **Literature Review:** Throughout this chapter we provide a comprehensive review of state-of-the-art methods for both the segmentation of LV and MYO structures as well as the process of feature extraction.

(3) **Data Understanding and Proposed Architecture:** Within this chapter, we make an introduction to both datasets used in the scope of this thesis, exploring the intrinsic differences between both. Still in this chapter, we also present an overview of the architecture of the proposed fully automatic pipeline.

(4) **Left Ventricle Segmentation:** In this chapter we explore the segmentation module of the proposed pipeline, giving particular focus to boundary enhancement, a crucial aspect for subsequent feature extraction.

(5) **Feature Extraction:** In this chapter, we explore the feature extraction of both global and local features, giving emphasis to our point pairing method developed to assess local features.

(6) **Conclusions** Finally, we present our final remarks, aiming to answer the proposed research questions. Additionally, we provide valuable suggestions for future research directions and areas of improvement.

CHAPTER 2

Literature Review

In this chapter, we review related work, which is critical to expand our knowledge of the problem we are assessing, as well as to understand what has already been done in relation to the subject of the study. To establish the foundation for this thesis, a preliminary review of the most pertinent papers within the domain of automatic cardiac diagnosis. as exemplified by Isensee et al.'s work [**15**], provided an initial insight into the workings of a fully automatic pipeline for disease classification. The primary objective of fully automatic methods is to eliminate the necessity for user intervention in tasks such as segmentation and feature extraction. As such, it is required that these methods effectively identify and delineate the targeted structures while also facilitating the extraction of pertinent features related to the segmentation outcomes.

In this literature review, our emphasis will initially be on appraising the current state-of-the-art techniques for short-axis MRI left-ventricular (LV) segmentation. Subsequently, the focus will shift towards the automated assessment of both global and local features that are relevant to the cardiac structures, aligning with the core objectives of this study.

2.1. Cardiac Segmentation

The correct segmentation of the cardiac structures is a crucial part of the process, as the quality of features extracted from the segmented structures is dependent on the accuracy of the segmentation. In this section, we explore the proposed segmentation methods for the LV and MYO structures. Given the small amount of data available on this topic, most recent studies rely on the few publicly available datasets for this problem. Therefore, we also go through the evaluation metrics and principal results achieved in each of these datasets, in order to identify the most accurate methods. To evaluate the viability and quality of a segmentation method, we have to look into the vast range of approaches available. In this section, we will go over the most common segmentation methods giving context to the presented examples of segmentation methods for publicly available datasets, presented in the next subsection.

2.1.1. Non-Deep Learning Methods

Petitjean and Dacher [**16**] reviewed 70 peer-reviewed publications on segmentation methods for LV and/or RV in Cardiac MRI. In this study, a division between weak and strong prior methods was proposed (see Table 2.1). Weak prior being the methods that use low-level information such as spatial, intensity, and weak anatomical information, and strong prior being based on statistical models, constructed or learned from a large number

of manually segmented images, usually not requiring user interaction. Although this work

TABLE 2.1. Non-Deep Learning segmentation methods reviewed by Petitjean and Dacher[**16**]

	Method
Weak Prior	image-based techniques pixel classification methods deformable models graph-based approaches
Strong Prior	shape prior based deformable models active shape and appearance models atlas based methods

paints the full picture of non-deep-learning methods applied to this area with practical examples, the methods themselves were not tested on the same dataset simultaneously therefore no practical comparison between all methods was defined. For more information regarding non-deep-learning methods applied to this field, we refer to Petijean and Dacher's work [**16**].

2.1.2. Deep Learning Methods

Deep Learning technologies emerged in the medical image segmentation field after 2013. Prior to this time, no deep-learning approaches were documented in cardiac MRI segmentation [**7**]. In 2019 Hesamian et al. [**17**] reviewed the most popular deep-learning techniques for medical image segmentation. Below, we present the main deep-learning architectures used to assess medical image segmentation issues:

Convolutional Neural Networks

As Hesamian et al. [**17**] describe, a Convolutional Neural Network (CNN) (Figure 2.1) consists of a stack of layers each performing a specific operation:

- Input Layer: Directly connected to an input image with the number of neurons equal to the number of pixels in the image;
- Convolutional Layers: Present the results of convolving a certain number of filters with the input data. These layers perform as feature extractors. The output of each convolution layer is considered an activation map;
- Pooling Layers: These layers help to reduce the dimensionality of the convolutional layer output and provide translational invariance, making the network more robust to slight shifts or distortions in the input data;
- Fully Connected Layers: Layers responsible for the extraction of high-level abstraction.

Recurrent Neural Networks

The fact that the Region of Interest (ROI) in medical images is, in MRIs and other similar medical procedures, distributed over multiple adjacent slices fits the type of data

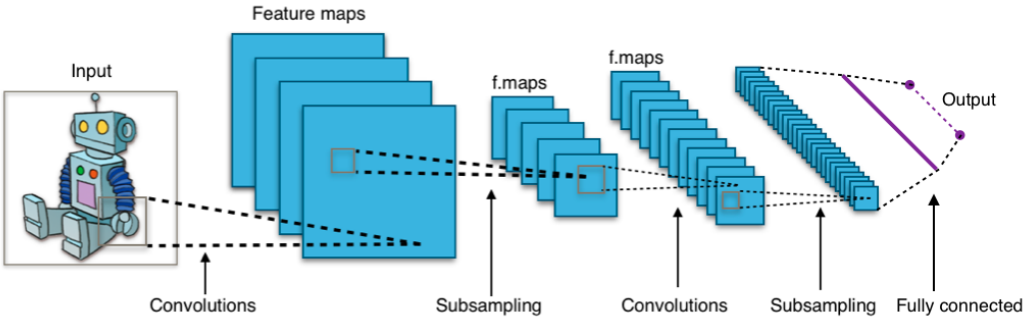

FIGURE 2.1. Convolutional Neural Network Architecture.

where the RNN succeeds. The recurrent neural network (RNN) can be aware of the correlation between successive slices. This type of structure is defined by two major sections:

- Intra-slice information extraction, which can be done by any CNN model;
- Inter-slice information extraction, which is done by the RNN.

Fully Convolutional Neural Networks

In the fully convolutional network (FCN) proposed by Long et al. [**18**], the last fully connected layer was replaced with a convolutional layer. This change allows for pixel-wise prediction instead of a patch-wise prediction proposed in CNN. If we compare Figures 2.1 and 2.2, it is visible that CNNs progressively reduce the representation path and provide one prediction per image. At the same time, FCNs follow the contracting path by an expansive one that reuses information to provide one prediction per pixel.

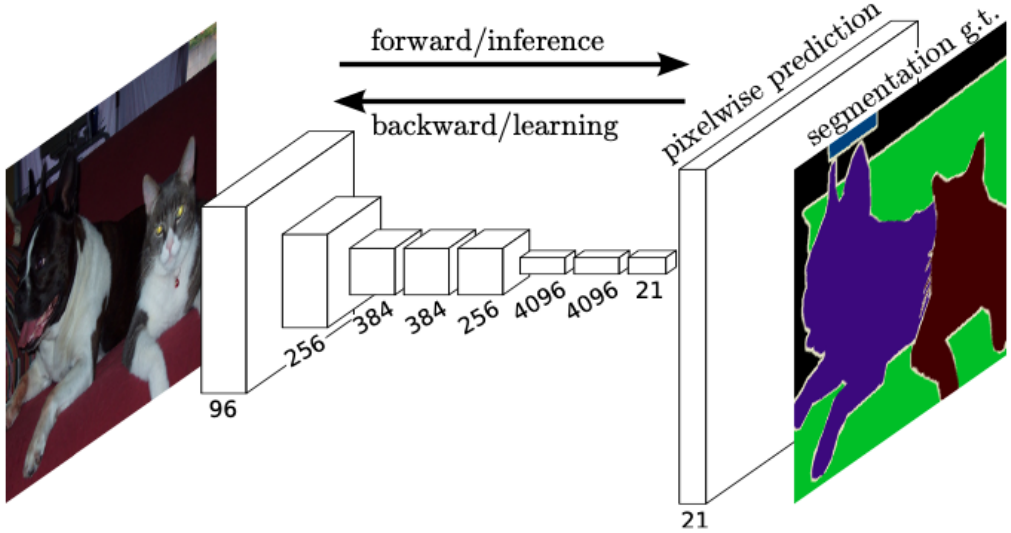

FIGURE 2.2. Fully Convolutional Neural Network Architecture [**18**].

Ronnerberger et al. [**19**] proposed one of the most well-known structures for medical image segmentation, the U-Net (Figure 2.3) based on the FCN architecture. The most important property of U-Net is the shortcut connections between the layers of equal

resolution in the analysis path to the expansion path. These connections provide essential high-resolution features to the deconvolution layers [**17**].

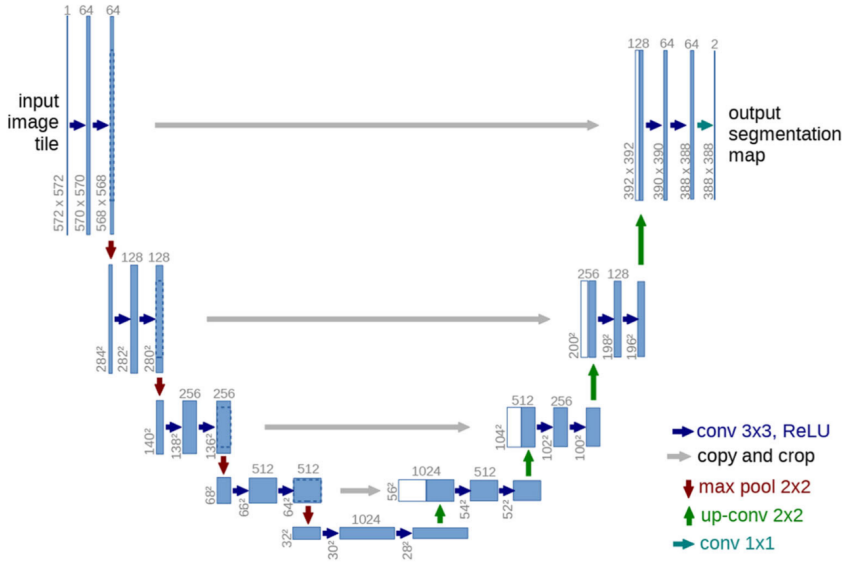

FIGURE 2.3. U-Net Architecture [**19**].

2.1.3. Evaluation Metrics

To fully understand and evaluate the results presented in the literature, there is a need to identify and provide context to the standard metrics used to assess segmentation accuracy:

- Dice similarity index:

$$D = 2(|Vuser \cap Vref|)/(|Vuser| + |Vref|) \tag{2.1}$$

  This metric calculates the overlap between the automatically segmented volume *Vuser* and the corresponding reference volume manually segmented *Vref*.

- Hausdorff surface distance:

$$d_{\mathrm{H}}(X, Y) = \max\left\{\sup_{x \in X} d(x, Y), \sup_{y \in Y} d(X, y)\right\} \tag{2.2}$$

  This metric measures the local maximum distance between two surfaces X and Y. Opposing previous approaches where Hausdorff surface distances (dH) were calculated for 2D images [**20**], in this case, the Hausdorff distance measures the maximum perpendicular distance between the automatic and manual contours [**21**]. However, in [**7**] a 3D dH approach was proposed which allows an intrinsic management of the missing segmentation problem on the end slices.

- Jaccard index:

$$J(A, B) = 2(|A \cap B|)/(|A \cup B|) \tag{2.3}$$

This metric measures the ratio of the overlap area between two sample sets A and B.

- Average Perpendicular Distance (APD):

  This metric calculates the distance from the automatically segmented contour to the corresponding one, manually drawn by an expert, and averaged over all contour points [**22**].

- Sensitivity (p), specificity (q), positive predictive value (PPV), and negative predivtive value (NPV):

$$p = T_1/N_1 \tag{2.4}$$

$$q = T_0/N_0 \tag{2.5}$$

$$PPV = T_1/(T_1 + F_1) \tag{2.6}$$

$$NPV = T_0/(T_0 + F_0) \tag{2.7}$$

  Where T_1 and T_0 are the numbers of correctly predicted pixels belonging to the object and background class, respectively. F_1 and F_0 represent misclassified pixels belonging to the object and the background classes as well. Finally, N_1 and N_0 are the total number of objects and background pixels, respectively [**5**].

2.1.4. Datasets and Principal Results

Five publicly available datasets of cardiac magnetic resonance (MRI) images have been highly accepted by the community in the last two decades, which allowed for drastic improvements in the area [**3, 4, 5, 6, 7**]. Given the small amount of publicly available data, most modern approaches have been based on one of these datasets. In this section, we aim to present an overview of datasets and proposed methods.

TABLE 2.2. Summary of publicly available datasets for Cardiac MRI segmentation

Name	**Year**	**Ground truth**
Sunnybrook[**3**]	2009	LV,MYO
STACOM [**5**]	2011	LV,MYO
MICCAI RV[**4**]	2012	RV
Kaggle [**6**]	2015	-
ACDC [**7**]	2017	LV,RV,MYO

Sunnybrook Cardiac MR Left Ventricle challenge

This dataset comprises 45 cardiac MRI images from four different different pathologies. Ground truth for segmentation was provided for both the endocardium and the epicardium.

Recent approaches to this data using deep-learning methods achieved the following results:

TABLE 2.3. Segmentation performance comparison for Sunnybrook Dataset

Method	**Dice metric**		**APD (mm)**	
	Endo	Epi	Endo	Epi
Tran. (2017) [**23**]	0.92	**0.96**	**1.73**	**1.65**
Avendi et al. (2016) [**20**]	**0.94**	-	1.81	-
Queiros et al. (2014) [**21**]	0.9	0.94	1.76	1.80
Ngo and Carneiro. (2014) [**24**]	0.89	-	2.26	-

In Table 2.3 we present the four highest-ranked segmentation methods applied to the dataset, that have achieved promising results in LV and MYO segmentation. Taking into account that all these results were achieved long after the publishing of the dataset, we have the deep learning methods from Tran and Avendi et al. and deformable models, active contour by Queiros et al., and level set by Ngo and Carneiro.

In this case, we can take the conclusion that deep learning surpasses other presented models and achieves state-of-the-art results. Through other dataset results the hypothesis of deep learning method superiority will be put to test.

The LV Segmentation Dataset MICCAI-STACOM

This challenge, once again, focuses on the LV segmentation method comparison [**5**]. The dataset provided in this challenge is composed of cardiac MRI images from 200 patients. However, manually drawn segmentation ground-truths were not delivered for training. Instead, the authors developed a framework that combined fully automatic and semi-automated approaches to achieve computed ground truths [**25**].

Once again Tran achieved the best results for fully-automatic segmentation with a Jaccard Index of 0.74. Margeta et al. implemented a Decision forest while Jolly et al. opted for a Deformable Registration model. Once again this results back the hypothesis that deep learning models achieve better results in comparison to other machine learning approaches. It is worth noting that for this dataset there was a Jaccard score of 0.84 [**26**], but this result was achieved with a semi-automatic method which is outside the scope of this study.

TABLE 2.4. Segmentation performance comparison for STACOM Dataset's fully-automatic methods

Method	**Jaccard Index**	**Sensitivity**	**Specificity**	**PPV**	**NPV**
Tran. (2017) [**23**]	**0.74**	0.83	**0.96**	0.86	**0.95**
Jolly et al. (2012) [**27**]	0.69	0.74	0.96	0.87	0.89
Margeta et al. (2012) [**28**]	0.43	**0.89**	0.56	0.50	0.93

The Right Ventricle Segmentation Dataset - MICCAI

This dataset developed for right ventricle (RV) segmentation method comparison is composed of 48 cardiac MRI images with manually drawn ground-truths. While the aim of this work is not right ventricle segmentation, the similarities in the problem, lead to

an interest in evaluating the approaches in segmentation methods for other structures. Therefore, we took into account the approaches and results tested in this data, as they help make a distinction between deep learning and previous approaches in a similar problem. As expected, at this point the Deep Learning approach continues to show its superiority against other methods.

TABLE 2.5. Segmentation performance comparison for the RV segmentation Dataset

Method	**Dice metric**		**Haussdorf distance** (mm)	
	Endo	Epi	Endo	Epi
Tran. (2017) [**23**]	**0.84**	**0.86**	**8.86**	**9.33**
Zuluaga et al. (2013)[**29**]	0.76	0.80	11.51	11.82
Wang et al. (2012) [**30**]	0.59	0.63	25.32	24.43

The 2015 Kaggle Second Annual Data Science Bowl

This dataset represents a training set of 500 patients but didn't provide manually segmented ground-truths. As reported by Bernard et al. [**7**], for this dataset, no summary paper was delivered. The outcome of the challenge however showed that the top-performing methods relied on deep learning technologies, specifically Fully Convolutional Neural Networks (FCN) [**31, 19**].

Automatic Cardiac Diagnosis Challenge

This challenge is the latest addition to publicly available datasets in this field. The training set is composed of 100 patients divided into 5 groups, 4 with different cardiac pathologies, and a healthy one. Further statistics and a review of all methods are presented by Bernard et al. [**7**].

TABLE 2.6. Segmentation methods evaluated during ACDC challenge [**7**]

Author/Reference	**Method**
Isensee et al.[**15**]	2D + 3D U-Net
Baumgartner et al.[**32**]	2D U-Net
Jang et al. [**33**]	2D M-Net
Zotti et al [**34**]	2D Grid-Net
Khened et al. [**35**]	Dense U-Net
Wolterink et al. [**36**]	Dilated CNN
Jain et al. [**37**]	2D U-Net
Rohé et al. [**38**]	SVF-Net
Tziritas-Grinias [**39**]	Levelset+MRF
Yang et al. [**40**]	3D U-Net

Most of the methods proposed by attendees implemented a deep learning architecture, most of which used a U-Net-based network, that analyzed the data slice by slice. The only exception was Tziritas and Grinias [**39**] which used a level-set method followed by

a Markov Random Fields (MRF) graph cut. Between the U-Net approaches, four papers re-used the U-Net architecture:

Baumgartner et al. [**32**] tested various hyperparameters, 2D and 3D convolutions, and two different loss functions, Dice loss and cross-entropy loss, achieving the best performance with 2D convolutions and cross-entropy loss. Isensee et al. [**15**] achieved the best performance by using an ensemble of 2D and 3D U-Nets, both networks trained with a Dice loss. Jain et al. [**37**] made a similar test to Baumgartner et al. with the same 2D and 3D convolutions and loss functions. However, their best performance was achieved with 2D convolutions and a Dice loss. Yang et al.[**40**] present a 3D U-Net with residual connections and pre-trained weights for downsampling. They also used a multi-class Dice loss. Wolterink et al. [**36**] implemented a CNN with encoder-decoder architecture.

Another four papers presented modified versions of the U-Net architecture:

Jang et al. [**33**] implemented an M-Net architecture that diverges from a regular U-Net by concatenating decoding layers of feature maps with others of previous layers. Khened et al. [**35**] implemented a dense U-Net. This method uses a Fourier transform to determine the ROI and computes an approximate radius and center of the LV with a Hough transform. They then implement a U-Net with dense blocks instead of convolution ones, with a sum of Dice and cross-entropy losses. Rohe et al. [**38**] developed a multi-atlas algorithm that first registers a target image with all training images. The registered label fields are then merged with a soft fusion method using pixel-wise confidence measures. The registration module implements an SVF-Net. Zotti et al. [**34**] developed a Grid-Net architecture which translates to a U-Net with convolutional layers along the skip connections. The model is trained with a four-term loss function.

TABLE 2.7. Segmentation performance comparison for the ACDC dataset, for both LV and MYO [**7**]

Method	**ED**				**ES**			
	LV		**Myo**		**LV**		**Myo**	
	D	d_H	D	d_H	D	d_H	D	d_H
Isensee et al.(U-Net)[**15**]	**0.968**	7.4	**0.902**	8.7	**0.931**	**6.9**	**0.919**	**8.7**
Baumgartner et al[**32**].	0.963	**6.5**	0.892	**8.7**	0.911	9.2	0.901	10.6
Jang et al.[**33**]	0.959	7.7	0.875	9.9	0.921	7.1	0.895	8.9
Zotti et al [**34**]	0.957	6.6	0.884	8.7	0.905	8.7	0.896	9.3
Khened et al.[**35**]	0.964	8.1	0.889	9.8	0.917	9.0	0.898	12.6
Wolterink et al.[**36**]	0.961	7.5	0.875	11.1	0.918	9.6	0.894	10.7
Jain et al.[**37**]	0.955	8.2	0.882	9.8	0.885	10.9	0.897	11.3
Rohé et al.[**38**]	0.957	7.5	0.867	11.5	0.900	10.8	0.869	13.0
Tziritas-Grinias [**39**]	0.948	8.9	0.794	12.6	0.865	11.6	0.801	14.8
Yang et al. [**40**]	0.864	47.9	-	-	0.775	53.1	-	-

From the results presented in Table 2.7, one can understand that the U-Net presented by Isensee et al. [**15**] achieved the top performance clearly surpassing other approaches.

2.1.5. U-Net Based Architecture

Taking into account, the various studies and challenges presented above, we can see a trend in deep learning-based methods outperforming older approaches. It is visible that architectures like U-Nets achieve state-of-the-art results second to none. The work presented by Isensee et al. surpasses all others in terms of dice score as well as Hausdorff distance. In this subsection, we dive deeper into the specific approach to this U-Net approach.

Architecture

The U-Net starts by implementing a preprocessing module responsible for resampling all volumes to account for varying spatial resolutions. The grey level information is also normalized to zero-mean and unit-variance. The proposed neural network comprises an ensemble of modified 2D and 3D U-Nets, with fairly similar structures, being the main difference having 2D and 3D convolutions. These networks are composed of an aggregating pathway followed by a localization path. These paths are connected in multiple stages, adding the abstract context of features to the corresponding local information.
Depicted in Figure 2.3 are feature extraction blocks (displayed in gray), these blocks are comprised of 2 3x3x3 convolutions, followed by both batch normalization and leaky ReLU nonlinearity.
The aggregation pathway is defined by 4 operations of pooling, starting with 26 feature maps (48 for the 2D U-Net due to lower memory requirements), which are doubled in each operation, leading to the bottom of the U-Net structure having 416 feature maps. Similarly, the upscaling process splits this feature maps through each of its 4 operations symmetrically. Due to low resolution on the z-axis both pooling and upscaling are two dimensional, only applied to x and y planes.
At the final steps of the network (the last 2 upscaling operations), deep supervision was added by generating low-resolution segmentation which is aggregated to the final extraction block. The final segmentation results from the sampling of the softmax outputs of each network to the original voxel resolution of the input image.

Training

The 3D model was trained for 300 epochs with 5-fold cross-validation through ADAM solver and pixel-wise categorical cross-entropy loss. Each epoch comprised 100 batches which were composed of four training examples, random crops of 224 x 224 x 10 voxels taken randomly from the training dataset in both ED and ES.

The 2D model was trained with a batch size of 10 and input patches of 352 x 352 pixels through multiclass dice loss:

$$\mathcal{L}_{dc} = -\frac{2}{|K|} \sum_{\kappa \in K} \frac{\sum_i u_i^\kappa v_i^\kappa}{\sum_i u_i^\kappa + \sum_i v_i^\kappa} \tag{2.8}$$

Where u is the softmax output of the network, v represents one-hot encoding of the ground truth segmentation, i is the number of pixels in the training patch, and $k \in K$ is

the classes.

Data Augmentation

Given the fact that there was limited data, the authors found a need to improve upon the dataset through data augmentation techniques. Between these techniques, we highlight mirroring along the x and y axes, random rotations, gamma correction, elastic deformations, and random increase of slice misalignment.

nnU-Net

Subsequently to the U-Net, Isensee et al. presented a novel deep learning framework [**41**], denominated nnU-Net, which provides a segmentation method adaptative to the provided dataset. Based on an automated analysis of the dataset, it automatically designs and executes a network training pipeline.

For the non-CT modalities (which encapsulate the scope of this work) the framework normalizes intensity values, subtracting the mean and dividing by the standard deviation. Furthermore, the neural network resamples all training data through a number of processes, which are described in depth. The architecture presents an ensemble of U-Nets: a 2D U-Net, a 3D U-Net, and a cascade of two 3D U-Nets (the first produces a low-resolution output which is defined by the second). The nnU-Net presents only slight differences to the above-referenced U-Net, namely padded convolution for output and input shape normalization, instance normalization, and Leaky ReLUs instead of ReLUs.

This flexible framework achieved state-of-the-art results, similar to those of the U-Net, in the ACDC dataset, posteriorly to ACDC's report publication.

2.2. Feature Extraction

In the assessment of left ventricular function, feature extraction is a critical process. Both global and local features can be inspected to evaluate the overall health and function of the cardiac structures [**42**].

Global features such as ventricular mass, volume, and ejection fraction are crucial in the diagnosis of cardiac conditions, however, such features can only give context to overall performance. On the other hand, local features such as left-ventricular wall thickness and thickening, allow for the local assessment of behavior that facilitates the identification of ill regions within the heart's structure. Multiple conditions can be identified by the correct assessment of wall thickness variations throughout the cardiac cycle, such as Hypertrophic Cardiomyopathy and Infarction [**43, 44**].

2.2.1. Wall Thickness

In clinical practice the typical approach is to assess wall thickness through visual inspection, leading this approach to be highly susceptible to variations given the difference in experience and inconsistencies of observers. To tackle this issue, and produce more accurate and reliable measurements, multiple semi-automatic and automatic approaches have emerged [**45, 46**].

Two prevalent methods for measuring cardiac anatomical thickness are usually employed. The first method involves the assessment of regional wall thickness [**47, 48**], which partitions the heart into several distinct regions and subsequently calculates the average thickness within each region. This approach reduces the need for labor-intensive manual measurements across the entire heart but provides only average values for myocardial regions. Therefore inhibiting practitioners from evaluating the full scope of thickness change throughout the cardiac structure. In contrast, the second method, dense wall thickness approach [**49, 50, 51**], provides location-specific measurements, offering a finer level of granularity in assessing myocardial thickness.

For this approach, two main methods are proposed: the center line method and myocardial tissue tagging. In the center line method, a line is drawn within the center of the LV wall, equidistant to the outer and inner borders of the LV myocardium. Subsequently, multiple chords are evenly spread around the muscle at specified intervals, perpendicular to the center line. Each chord's length variation between systole and diastole is representative of the local wall thickness of that segment [**2**]. This method has known limitations namely the lack of resilience to different angle shots in cardiac MRI slices, meaning that a slightly tilted image could result in an overestimation of wall thickness. Another limitation is that the center line doesn't take through-plane motion into consideration through the cardiac cycle [**52**].

Tissue tagging on the other hand is a proposed method in which tagline separations, intersections, or line pair alterations allow the measure of wall thickness changes throughout the cardiac cycle [**53**].

In a recent study [**54**], a more reliable method for measuring myocardial thickening in cardiac MRI images was introduced. This was achieved by solving a partial differential Laplace equation. Despite this advancement, there is still a need for manual adjustments by clinical experts to minimize segmentation errors in the estimation of wall thickness. The partial differential equation (PDE) is used to establish correspondences between points on segmented wall borders. It's worth noting that solving this PDE, unlike prior methods, is highly computationally intensive. Another approach for estimating wall thickness was proposed by leveraging deep learning capabilities [**55**]. This method includes a rapid solver for estimating thickness from binary annular shapes and an end-to-end deep learning network for directly estimating thickness from raw cardiac images, leveraging manually adjusted PDE-calculated thicknesses to train the algorithm.

2.2.2. Wall Thickening

Myocardial thickening also referred to as wall thickening is a measure that represents the change in myocardial thickness throughout the cardiac cycle. This feature, which derives from the wall thickness calculation, can be calculated both in absolute and in percentage. The literature [**56**] presents data that supports that this feature is very relevant in the assessment of some LV conditions namely infarction.

2.2.3. Ejection Fraction

The literature proposes two main techniques for the assessment of left-ventricular ejection fraction for cardiac MRI images, Simpson's rule technique [**57**] and area-length technique [**58, 59**]. The Simpson's rule technique involves calculating the left-ventricular area of each short-axis slice and then multiplying this value by the thickness of the slice. This approach is based on the principle of summation of the volumes of individual slices. The area-length technique assumes that the left ventricle is prolate ellipse-shaped. This approach only requires one or two slices depending on the single-plane or biplane method, which significantly reduces analysis time. Some cardiomyopathies may change LV configuration, which may challenge the assumption that LV structure can be represented through an ellipse. Hence, Simpson's rule is often considered more accurate as it doesn't rely on assumptions about the ventricular shape.

CHAPTER 3

Data Understanding and Proposed Architecture

In this chapter we analyze the different datasets chosen for the evaluation and validation of the proposed pipeline, going through the population's characteristics and file format specific to each set. Furthermore, we make a brief overview of the proposed architecture, going through high-level definitions of the multiple modules that compose the automatic pipeline.

3.1. Data Understanding

To validate our Automatic Pipeline we used 2 different cardiac Magnetic Resonance Imaging (MRI) datasets, for different stages of the development. We first used Automatic Cardiac Diagnosis Challenge (ACDC) dataset [**7**] where we developed our first approach and proof of concept. Later we also validated our proposal in a private dataset developed in consortium with Affidea Caselas. The number of patients in each dataset is summarized in Table 3.1.

Table 3.1. Dataset High-level description.

Source	**Number of Patients**	**Availability**
ACDC [**7**]	150	Public
Private Dataset	30	Private

3.1.1. Public Dataset

The ACDC dataset, developed by the University Hospital of Dijon, joins 150 short-axis MRI exams from 150 different patients, evenly distributed between healthy and 4 pathological subgroups. In each exam additional info, such as weight, height and End of Diastole (ED) and End of Systole (ES) instants were provided. The data was provided in two different sets, a 100 training set and a 50-patient test set.

System Description and Variations

These exams were executed within a 6-year period with 2 MRI scanners with different magnetic strengths:

- Siemens Area, with 1.5 T strength;
- Siemens Trio Tim, with 3.0 T strength.

Each exam was exported as a series of short axis slices, that cover the Left Ventricle (LV) from the base to the apex, in Neuroimaging Informatics Technology Initiative (NIFTI) format. Given the circumstances in which the images are taken, there are some variations to each exam's image properties:

- Thickness between slices can vary between 5 and 10 mm;
- Spatial resolution can go from 1.37 to 1.68 mm2/pixel;
- Each cardiac cycle can range between 28 to 40 3D images.

Dataset Population

The 150 patients are evenly divided into 5 subgroups (30 each):

- NOR: Healthy/Normal subjects;
- MINF: Previous Myocardial infarction, identified by an Ejection Fraction (EF) below 40% and abnormal contraction on MYO segments;
- HCM: Hypertrophic cardiomyopathy, where LV mass surpasses 110 g/m^2 and with multiple MYO segments with a thickness above 15 mm in diastole;
- ARV: Abnormal Right Ventricle, RV volume superior to 110 mL/m^2 and a right ventricular EF below 40%.

It is worth noting that right ventricular issues are outside the scope of this study, therefore, this subgroup was excluded from the process.

3.1.2. Private Dataset

This dataset was retrieved and pseudo-anonymized, following the guidelines of Affidea's ethical committee. It consists of 30 patients, equally divided into two distinct pathological subgroups and a healthy group. These patients underwent thorough evaluation and classification by experts in the field.

It will serve primarily for the feature extraction algorithm, as it does not provide ground truth information for segmentation tasks. Therefore, it will be employed as a validation dataset, contributing to the demonstration of the utility of this tool in assisting with the diagnosis of these medical conditions.

Provider

Affidea is the leading provider of advanced diagnostic imaging, outpatient, and cancer care services in Europe, operating 328 centers in 15 countries. This dataset was extracted from one of Affidea's centers in Caselas.

Dataset Population

The 30 patients were retrieved from the MRI center's database, in Digital Imaging and Communications in Medicine (DICOM) format, evenly distributed between 3 groups (10 patients each):

- NOR: Healthy/Normal subjects;
- DCM: Patients with dilated cardiomyopathy;
- HCM: Patients with hypertrophic cardiomyopathy.

Dilated Cardiomyopathy

Dilated cardiomyopathy is defined by the presence of left ventricular dilatation and contractile dysfunction, in the absence of abnormal loading conditions and severe coronary artery disease [**60, 61**]:

- **Left Ventricular Dilation**: In this condition, the left ventricle suffers an expansion in internal volume that impairs the blood ejection function;
- **Contractile Dysfunction**: Also associated with the disease is a significant decrease in contractile strength particularly in the myocardium.

Both these symptoms lead to a reduction in ejection fraction contributing to a reduced cardiac output and compromised circulation.

Hypertrophic Cardiomyopathy

Hypertrophic Cardiomyopathy is a condition, usually inherited, that consists of excessive thickening in the left ventricular wall impeding blood flow from circulating properly.

3.1.3. File Format

The datasets mentioned above were supplied in different file formats. The ACDC dataset is provided in NIFTI [**62**] image format, while the Affidea Caselas dataset is in DICOM [**63**] image format. In this sub-section, we present the main differences between both file structures with the goal of providing extra context over the processing of both datasets.

DICOM

DICOM is considered the standard file format for medical imaging data acquisition. As most DICOM files involve a single slice from an acquisition [**64**], it is clear that this data structure is not the most efficient way of analyzing multi-dimensional images.

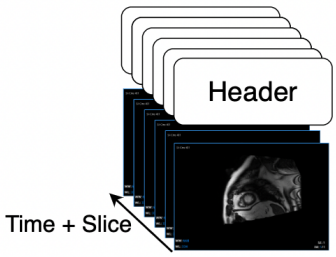

FIGURE 3.1. DICOM structure.

NIFTI

This format is a direct descendent of the ANALYZE format, both were developed under the premise of storing grouped multi-dimensional biomedical data in a single file. In the case of ANALYZE, there was a binary file with the heather information and another containing the images. NIFTI improved upon ANALYZE, allowing both the header and the 3 or 4-dimensional data to be stored together.[**64**]

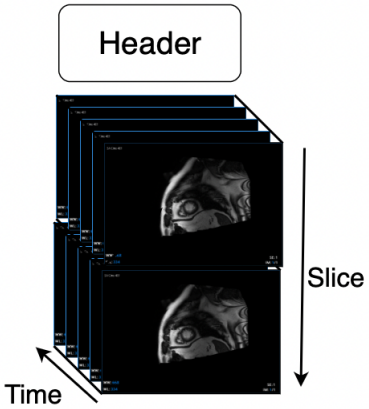

FIGURE 3.2. NIFTI structure.

As NIFTI brings the benefit of storing 3 or 4-dimensional data in a single file, it is shown to be simpler and faster to load and process.

3.2. Proposed Architecture

In this work we propose an automatic solution to aid in the diagnosis of specific cardiac conditions. While there are promising developments made in the various fields of medical image analysis, there seems to be a lack of approaches that focus on leveraging the available technology to propose fully automatic tools.

As such, our proposed architecture comprises three modules: Data Pre-processing, Segmentation, and Feature Extraction. These modules operate independently, allowing for the interchangeability of each step in the pipeline, described in the following chapters:

(1) **Data pre-processing**: In this stage of the pipeline we process the raw data, starting with image format conversion, to normalize datasets and fit the needs of the following segmentation layer.

(2) **Left Ventricle Segmentation**: This stage is composed of two layers:
   (a) **Base Segmentation Layer** a first segmentation approach with a pre-trained network that delivers state-of-the-art results in LV and MYO segmentation. The nnU-Net was the algorithm of choice for the first layer of segmentation of our proposed model.
   (b) **Enhanced Boundary Definition** a double active-contour segmentation, that aims to improve upon the prior segmentation in capability of feature extraction. Here two active contours are employed to refine the shapes of the segmented LV and MYO boundaries.

   The output of this process comprises two active-contour boundaries and a state-of-the-art segmentation, that can be leveraged for feature extraction.

(3) **Feature extraction**: In the concluding phase of our workflow, we process the output of the segmentation stage to extract relevant features for cardiac condition diagnosis, leveraging the enhanced boundary definition to achieve more accurate and consistent characterization of relevant local features in the cardiac cycle.

Here we propose a novel point-pairing method, for accurately identifying and measuring segments along the cardiac muscle.

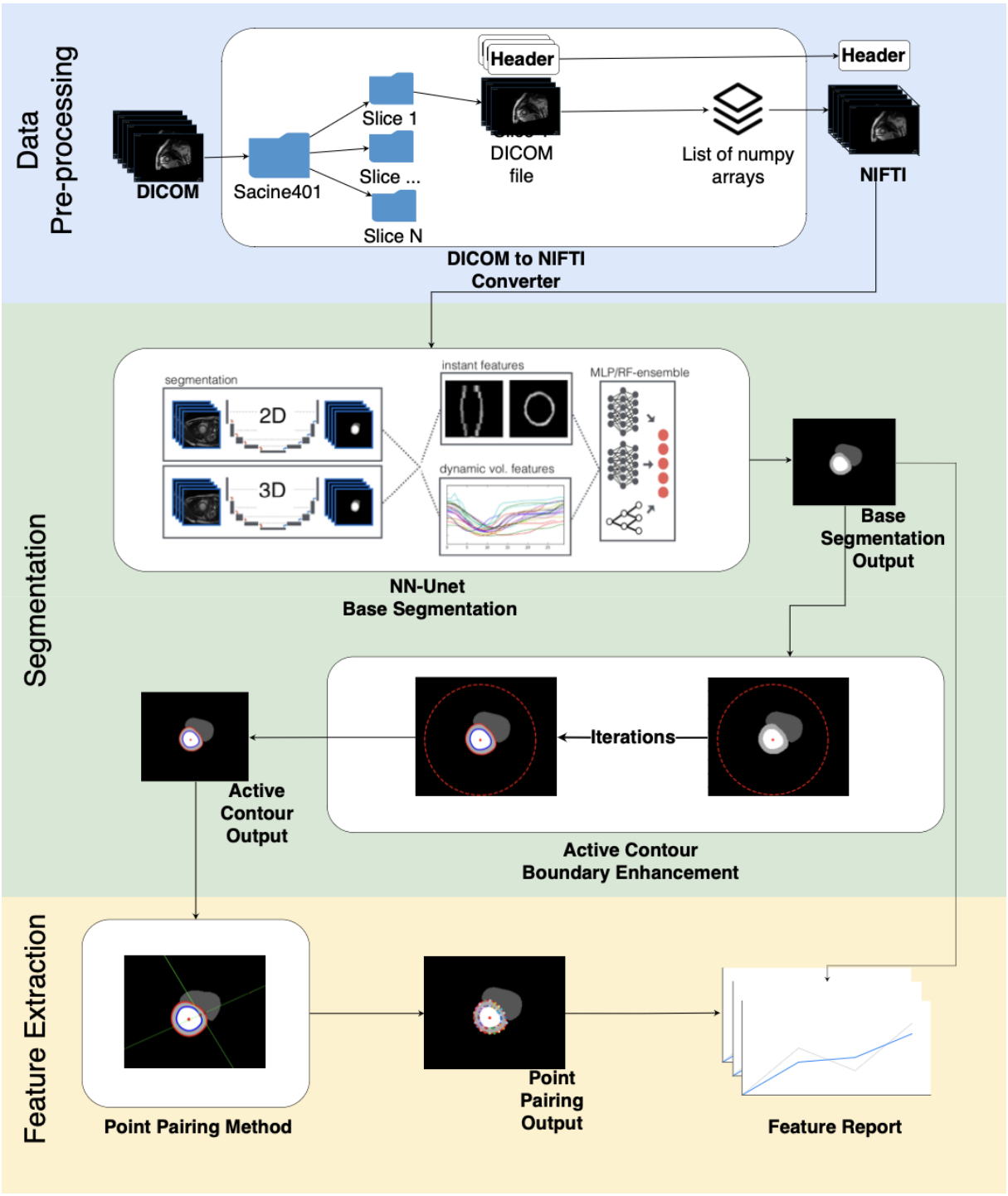

FIGURE 3.3. Automatic Pipeline.

CHAPTER 4

Left Ventricle Segmentation

In this chapter, we go through each stage of the segmentation process. Starting with a pre-processing stage, critical to fit the needs of the proposed segmentation pipelines, where data normalization takes place, allowing the conversion of DICOM [**63**] images to NIFTI [**62**] file format. Following the data pre-processing, we present a segmentation pipeline comprised of a base segmentation layer, through the state-of-the-art nnU-Net algorithm, followed by a boundary enhancement layer, where a double active-contour aims to refine the shapes of the segmented structures providing an optimized segmentation for feature extraction.

4.1. Data Normalization

This pre-processing module aims to normalize the data in such a fashion that allows for the pipeline to intake different types of file formats for cardiac Magnetic Resonance Imaging (MRI). In the data understanding section (see 3.1.3) we present the argument that NIFTI has advantages in what concerns multi-dimensional image analysis and therefore was chosen as the default file format for the proposed approach. While there are some available tools that could be used to automate this process, some experiences proved that their reliability was not to the standard that was expected.

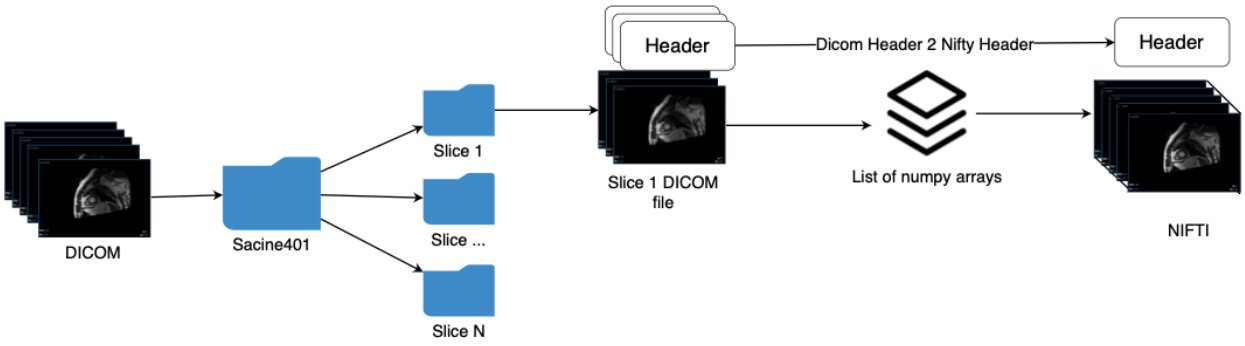

FIGURE 4.1. Data Pre-processing.

Therefore we propose a converter that processes each DICOM single slice file and produces 3D NIFTI images. This converter can be divided into 3 stages:

(1) **Data Sort**: Each image is processed and saved in a specific folder categorized by both the type of cut and slice height.

(2) **Image Conversion**: The previously defined folders are iterated and each slice folder is converted into a list of numpy arrays (1 per frame). It is also at this stage that DICOM headers are iterated and critical data is retrieved.

(3) **NIFTI export**: A 3D NIFTI file is saved with the Header info and image array list.

4.2. Base Segmentation Layer

The algorithm of choice for the base segmentation layer of the pipeline was the nnU-Net [**41**]. This segmentation framework provides a model pre-trained on Automatic Cardiac Diagnosis Challenge (ACDC) [**7**]. Therefore no further efforts were required for the segmentation of short-axis slices. While this model has proven to provide state-of-the-art results in LV and MYO segmentation, there are some limitations to its results. The first issue relies on edge granularity which is an issue as cardiac structures tend to follow smooth patterns, and it proves to be more difficult to extract features from granular instead of continuous boundaries. Furthermore, being a deep-learning algorithm, there are edge cases in which it can produce anatomically impossible segmentations.

4.3. Enhanced Boundary Definition

In the preceding section, a base segmentation layer is defined, leveraging the nnU-Net capabilities. The output of this layer brings some limitations, such as edge granularity and edge cases of anatomically impossible segmentations. The edge granularity is especially relevant, as cardiac structures tend to be smooth by nature. Furthermore, the lack of smoothness presents a more complex issue for local feature assessment. Therefore, to face these limitations, we present a boundary enhancement layer, comprised of two active contours. The focus of these active contours is to enhance boundaries to a smoother shape, removing granularity while ensuring minimal losses in accuracy. Additionally, this approach addresses part of the issue of anatomically impossible segmentations, as both the MYO and LV structures need to be fully segmented (meaning that both are enclosed) for the active contours to contract to their shape.

4.4. Implementation

In this section, we explore the implementation of the active contour model, covering the selection of the appropriate tools and the refinement of each parameter. This modeling process will be conducted iteratively, starting with the determination of the optimal number of points. Subsequently, we will focus on enhancing the segmentation of the most complex regions. Finally, we will fine-tune the parameters related to edge repulsion and brightness attraction to achieve the highest level of accuracy possible. To assess the quality of this enhancement the dice score of the base segmentation will be used as a baseline to which the enhanced segmentation shouldn't deviate significantly.

4.4.1. Scikit-image Active Contour

For this thesis, the library of choice for boundary enhancement was Scikit-image, a renowned Python library, known for its ease of use and integration with the scientific stack. The library provides an active contour model that offers a customizable platform for boundary detection and smoothing (the aim of the current segmentation stage). Its

integration with Numpy, Scipy, and Matplotlib streamlines the workflow for data analysis and visualization.

We make a brief introduction to the active contour's parameters to later explore the settings and tuning:

(1) **snake - Initial Contour**: - The `snake` parameter represents the initial contour or curve that will evolve to fit the object's boundary.

(2) **alpha - Elasticity Parameter**: - The `alpha` parameter controls the elasticity of the contour. A higher value makes the contour more elastic, allowing it to deform easily, while a lower value results in a more rigid contour.

(3) **beta - Smoothness Parameter**: - `Beta` governs the smoothness of the contour. It affects how much the contour resists bending or curving. Higher `beta` values yield smoother contours, while lower values allow for more pronounced curves.

(4) **gamma - Time-step**: - The `gamma` parameter controls the time-stepping behavior during the optimization process, determining the size of each iteration's time step. Higger values of `gamma` result in larger updates in each iteration, however faster convergence may introduce instability, in an edge case resulting in the collapse of the contour. Conversely, lower `gamma` values will lead to smaller but steadier updates through each iteration.

(5) **max_iterations - Maximum Iterations**: - `Max_iterations` specifies the limit on the number of iterations the algorithm should perform.

(6) **convergence - Convergence Criteria**: - The `convergence` parameter sets a stopping criteria based on the change in the contour between consecutive iterations. When the change falls below this threshold, the algorithm terminates.

(7) **w_line - Brightness Attraction Weight**: The `w_line` parameter controls the attraction of the contour to regions of brightness. A positive value attracts the contour toward regions of higher brightness, while a negative value attracts the contour toward darker regions in the image.

(8) **w_edge - Edge Repulsion Weight**: The `w_edge` parameter governs the repulsion of the contour from edges or sharp transitions in the image. A positive value pushes the closer to edges, while a negative value repels the contour from the edges.

(9) **boundary_condition - Boundary Conditions**: The `boundary_condition` parameter determines how the contour interacts with the boundaries of the image. It can take on several values:

- `'periodic'`: This option attaches the two ends of the snake, creating a continuous loop. It is suitable for cases where the contour should wrap around the image boundaries;
- `'fixed'`: This setting holds the endpoints of the contour fixed in place, preventing them from moving. It is useful when the contour should not extend beyond certain boundaries;

- `'free'`: The 'free' option allows unrestricted movement of the contour's endpoints, enabling them to move freely within the image. This is suitable for scenarios where the contour should adapt to any object shape;
- `'fixed-free'` or `'free-fixed'`: These options combine 'fixed' and 'free' behaviors for the two endpoints, respectively. They allow one endpoint to be fixed while the other is free to move.

4.4.2. Initial Shape

To grant that the active contour model fits in our fully automatic pipeline, there is a need to automate the initialization process of the model. Here the model requires an initial shape, which will be the starting point for the active contour segmentation. The shapes will then contract into the boundary of the Left Ventricle (LV) and Myocardium (MYO), enhancing the final output.

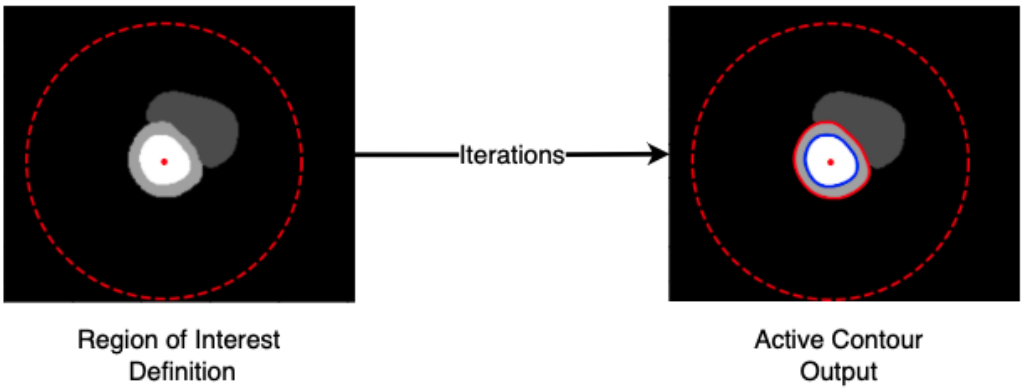

FIGURE 4.2. Active contour Region of Interest and Output.

To automate this process we first calculate the center of mass of the previously segmented LV, as that is the object of this segmentation process. Below we present the equation for both coordinates:

$$x = \frac{\sum_{i \in W} m_i * x_i}{M} \tag{4.1}$$

$$y = \frac{\sum_{i \in H} m_i * y_i}{M} \tag{4.2}$$

Where M is the sum of pixel values, is comprehended between 0 and the width of the matrix for the x coordinate and the height for the y coordinate, m_i is the pixel value at i, x_i and y_i are the x and y coordinate at i respectively.

Subsequently to this calculation solving the shape positioning, there is a need to turn to the shape's size and number of points, both critical to the snake's performance and robustness. Each snake's first shape should be a circle broad enough to include all regions where there is a possibility of being a segmented structure.
In Figure 4.2 we can visualize the artifacts mentioned above, and their contribution to the final segmentation.

4.4.3. Number of Points

The choice of the number of points along the MYO and LV contours plays a critical role in achieving a balance between efficiency and accuracy in this segmentation process. The optimal number of points can vary depending on several factors, including the resolution of your images, the complexity of the segmented shape, and the specific goal of the segmentation, in this case, the features that will be extracted. Smaller numbers of points will lead to a less accurate and more circular/stiff shape representation, while higher numbers of points will lead to a more granular and edgy/malleable shape. The smoothness parameter `beta` can be used to improve the result in the case of the latter. From an efficiency standpoint, fewer points will also lead to faster segmentation. To determine the ideal number of points for the active contour method, we initiated our investigation with a preliminary test.

In this initial approach, we consider three different sets of numbers of points: 100, 500, and 1000. This range of point counts allows the assessment of the impact of point density on the accuracy and efficiency of the segmentation process. This approach will be evaluated both from a visual standpoint as well as through the `dice metric`, as well as the volumetric error(Err) which stands for the difference between the predicted volume of the slice and the real volume, calculated in ml. Basal, mid, and apex slices will be used in the evaluation process to make sure that the model is tuned with the different characteristics of the segmented structures in mind.

This systematic evaluation aims to identify a suitable number of points for our specific objective. It is worth noting that some other values need to be set to accurately understand which number of points is the best choice, namely the `gamma` parameter for defining different time steps according to the size of the snake, this value was set based on trial and error in a specific image and then generalized for the setting. The input image is also passed through a Gaussian filter, reducing noise and detail. This can help to highlight the edges of the object of interest. The Gaussian filter has a `sigma` parameter, which dictates the determines the extent of the smoothing, lower variances will result in the filter affecting smaller areas and vice-versa. This parameter helps stabilize and smooth snakes with higher numbers of points.

The first test approach was executed by applying the snakes to the ground truth images in the ACDC training dataset. This action by itself does not represent a segmentation model, instead, we only aim to find the best settings for the active contour that will lead to fewer losses in shape and dimension. Below we present the results of the study for the base, mid, and apex slices respectively:

After evaluating the results of tables 4.1 to 4.3, we can confidently assume that LV and MYO number of points, for a higher accuracy segmentation differ. This might be related to the size difference between the two structures. The settings for LV segmentation that yielded the best results in all three slices were 100 points with smaller values of `sigma` (sigma = 1). In the Myo segmentation, the settings that best fit the model were 500

TABLE 4.1. Results for number of points experience - Basal Slice

Gamma	Num. of Points	Gaussian Sigma	Dice LV/ Err LV	Dice Myo / Err Myo
0.005	100	1	**0.9690 / -0.5579**	0.9272 / -3.4928
0.0002	500	1	0.9410 / -0.3138	0.9572 / -0.2684
5e-05	1000	1	0.9325 / -0.5115	0.9546 / -0.4757
0.005	100	2	0.8525 / -4.4169	0.3918 / -28.5477
0.0002	500	2	0.9492 / -0.3785	**0.9678 / -0.8948**
5e-05	1000	2	0.9401 / -0.4555	0.9560 / -0.8001
0.005	100	3	0.6716 / -9.9360	0.2879 / -31.6360
0.0002	500	3	0.9544 / -0.8584	0.9433 / -2.8240
5e-05	1000	3	0.9415 / -0.7177	0.9408 / -2.5162

TABLE 4.2. Results for number of points experience - Mid slice

Gamma	Num. of Points	Gaussian Sigma	Dice LV / Err LV	Dice Myo / Err Myo
0.005	100	1	**0.9844 / -0.511**	0.9400 / -3.4354
0.0002	500	1	0.9539 / -0.2747	0.9715 / -0.2899
5e-05	1000	1	0.9430 / -0.4887	0.9681 / -0.4350
0.005	100	2	0.8771 / -4.0529	0.4355 / -26.8639
0.0002	500	2	0.9613 / -0.4010	**0.9808 / -1.0351**
5e-05	1000	2	0.9524 / -0.3137	0.9697 / -0.9268
0.005	100	3	0.6483 / -10.8348	0.3225 / -30.0569
0.0002	500	3	0.9663 / -0.8608	0.9531 / -3.0069
5e-05	1000	3	0.9522 / -0.6808	0.9564 /-2.5960

TABLE 4.3. Results for number of points experience - Apex slice

Gamma	Num. of Points	Gaussian Sigma	Dice Lv / Err Lv	Dice Myo / Err Myo
0.005	100	1	0.8551 / 0.3943	**0.9666 / -0.5451**
0.0002	500	1	0.7972 / 0.1056	0.9376 / -0.2869
5e-05	1000	1	0.7765 / 0.1028	0.9276 / -0.3421
0.005	100	2	**0.8781 / -0.5119**	0.8423 / -2.5767
0.0002	500	2	0.8628 / -0.3128	0.9310 / -0.8275
5e-05	1000	2	0.8273 / -0.2915	0.9123 / -0.8427
0.005	100	3	0.7824 / -0.5729	0.7537 / -4.0443
0.0002	500	3	0.8676 / -0.3254	0.8785 / -1.6545
5e-05	1000	3	0.8328 / -0.3546	0.8475 / -1.8549

points with some higher values of `sigma` (sigma = 2). We can also identify that while this first stage yielded good results in both the basal and mid slices, the model has shown poor results in the apical slices, specifically in the LV segmentation, for the settings. Maintaining the theory that the ideal number of points will differ based on the size of the structure we aim to segment, we can assume that further testing with lower numbers of points may improve the overall results in these types of slices. It is also worth noting that for this specific test, the average encompasses both results from End of Diastole (ED) and End of Systole (ES). As explained in the literature (see 2.1.1) there is also a big difference in shape and size, for the same structures in these two moments. A distinction may have to be made, between both for optimal results.

4.4.4. Apical Slices Improvement

As stated above, apical slices have yielded the worst results in the first experience. As a hypothesis, we know that apical slices comprise smaller structures to segment, and propose there is a correlation between the model's poor performance and its size. Therefore this section delves into the specific case of apical slices, by trialing lower numbers of points for a more accurate segmentation. While valid in all slices, apical slices present the most challenging segmentation challenge, as apical slices at ES can be achieved in very small sizes.

We will start by looking at examples of good and bad performance within these types of slices and then try to generalize a solution to the issue. For this purpose, we used a random patient (patient 069) from the training set of the ACDC dataset and applied both MYO and LV active contours with the best settings for apical slices.

FIGURE 4.3. Apical ED and ES slice comparison.

TABLE 4.4. Results for patient 69 at both ED and ES

Patient	Frame	Slice	Cardiac Cycle Stage	LV Dice Score / LV Vol Error
69	01	apical	ED	0.9723 / -0.1221
69	12	apical	ES	0.8781 / -0.5119

Evaluating the output of the best settings for both MYO and LV in apical slices, seen in Figure 4.3, we can see that the LV is being correctly identified, however by evaluating the accuracy in Table 4.4, we identify that the dice score of this segmentation is below the standard we expect. Upon further investigation, we found that for the specific patient's apical slices, at ES the LV area comprised 43.9 mm (18 pixels) while at ED it was 314.9 mm (129 pixels). For the algorithm application, the area in pixels is more relevant and standard for normalizing rules. From our experience in previous tests, smaller structures tend to be more accurately segmented with smaller numbers of points. Therefore, in Table 4.5, we present the results for an experience in which lower numbers of points were applied to these structures. This experience targeted both ED and ES stages, and presented results for this two stages as well as the aggregation of both stages (Combo).

TABLE 4.5. Number of points experience for apical slices

Gamma	Points	Sigma	Cardiac Cycle Stage	Dice LV	Err Lv
0.005	100	1	ED	0.9797	-0.1894
0.005	100	1	ES	0.7239	1.0088
0.005	100	1	Combo	0.8551	0.3943
0.005	100	2	ED	0.9068	-0.8737
0.005	100	2	ES	0.8478	-0.1310
0.005	100	2	Combo	0.8781	-0.5119
0.005	75	1	ED	0.9562	-0.4142
0.005	75	1	ES	0.9172	-0.1310
0.005	**75**	**1**	**Combo**	**0.9372**	**-0.2650**
0.005	75	2	ED	0.8289	-1.7645
0.005	75	2	ES	0.8139	-0.2384
0.005	75	2	Combo	0.8217	-1.0210
0.005	50	1	ED	0.7907	-2.0820
0.005	50	1	ES	0.8656	-0.1771
0.005	50	1	Combo	0.8272	-1.1539
0.005	50	2	ED	0.3537	-4.6043
0.005	50	2	ES	0.6650	-0.4441
0.005	50	2	Combo	0.5053	-2.5776

Assessing the active contours with a higher number of points, we can see that there is a big discrepancy between ED and ES stages more prominent in lower values of `sigma`. After further evaluation of Table 4.5, we can suggest that while 100-point active contours prove to be the most accurate for ED phase in apical slices, the most robust solution is the 75-point active contour, yielding a Dice score of 0.9172 for ES phase while only loosing around 2.3% on the ED phase, in comparison to the top performer for that phase. These settings yield an average Dice score of 0.9372 for apical slice LV segmentation. In Table 4.6, we provide a breakdown of the current accuracy per slice during the second iteration of our modeling process. Notably, we observe an approximately 6% enhancement in the overall performance of apical slice results, bringing them closer to the others.

TABLE 4.6. Apical slice improvement results

Slice	Dice Lv / Err Lv	Dice Myo / Err Myo
Basal	0.9690 / -0.5579	0.9678 / -0.8948
Mid	0.9844 / -0.511	0.9808 / -1.0351
Apical	0.9372 / -0.2650	0.9666 / -0.5451

4.4.5. Edge Repulsion

Upon closer examination of the previous segmentation results, it became apparent that certain active contours neglected to capture edges and instead converged toward the structures' inner regions. To enhance the performance and accuracy of our model, we propose a test with multiple values of the `w_edge` parameter, described above, to guide the contours towards the edge of the structures. All prior tests have been executed with

the default `w_edge = 1`. We present in Table 4.7 a subset of the results pertaining to statistically relevant values.

TABLE 4.7. Edge repulsion settings and results

Slice	w_edge	Dice Lv / Err Lv	Dice Myo / Err Myo
Basal	1	0.9690 / -0.5579	0.9678 / -0.8948
Basal	2	**0.9911 / -0.2808**	**0.9722 / -0.8851**
Basal	3	0.9835 / -0.2773	0.9713/ -0.8622
Mid	1	0.9844 / -0.5110	**0.9808 / -1.0351**
Mid	2	**0.9911 / -0.2759**	0.9709 / -1.0481
Mid	3	0.9821 / -0.2761	0.9718 / -0.7572
Apical	1	0.9380 / -0.1594	0.9666 / -0.5451
Apical	2	**0.9561 / -0.1343**	0.9816 / -0.2736
Apical	3	0.9366 / -0.1317	**0.9852 / 0.2068**

Upon analyzing Table 4.8, it becomes evident that LV segmentation consistently exhibits improved performance with a `w_edge = 2`. However, the MYO segmentation results can vary significantly depending on the specific slice being analyzed. Nonetheless, it is noteworthy that the overall loss of information resulting from the application of active contours remains minimal at this stage of our study.

TABLE 4.8. Edge repulsion improvement results

Slice	Dice Lv / Err Lv	Dice Myo / Err Myo
Basal	0.9911 / -0.2808	0.9722 / -0.8851
Mid	0.9911 / -0.2759	0.9808 / -1.0351
Apical	0.9561 / -0.1343	0.9852 / 0.2068

4.5. Brightness Attraction

As a last stage of our fine-tuning process, we look at the average volume error, present in Table 4.8. Upon close inspection, the data suggests that overall the volume estimate is on average below the actual volume of the segmented structure. At this stage, we will focus on expanding the segmentation slightly in order to improve this metric while trying not to over-segment. While higher values of `w_line` will guide the segmentation towards brighter regions, which are the object of the segmentation, using negative numbers will drive the contour towards darker regions, closer to the edge of the structure.

The data in Table 4.9 suggests that only apical slices have a significant improvement in accuracy by using the `w_line` parameter. With this, we conclude the fine-tuning process of the boundary enhancement model.

4.6. Results

For the final evaluation of the proposed segmentation layer, we used the test set, from the ACDC dataset. The first segmentation layer, comprised of the pre-trained nnU-Net was applied to the test set, followed by the active contour models for both MYO and LV

TABLE 4.9. Brightness attraction settings and results

Slice	w_line	Dice Lv / Err Lv	Dice Myo / Err Myo
Basal	0	**0.9911 / -0.2808**	**0.9722 / -0.8851**
Basal	-0.5	0.9890 / 0.2976	0.9697 / 2.1786
Basal	-1	0.9694 / 0.9771	0.9347 / 5.0034
Mid	0	**0.9911 / -0.2759**	**0.9808 / -1.0351**
Mid	-0.5	0.9887 / 0.2949	0.94071 / 4.24532
Mid	-1	0.9684 / 0.9545	0.8836 / 8.8400
Apical	0	0.9561 / -0.1343	0.9852 / 0.2068
Apical	-0.5	**0.9714 / 0.0797**	**0.99342 / 0.05736**
Apical	-1.0	0.9161 / 0.3475	0.9807 / 0.3165

boundaries. The Dice score and average error were recorded for both stages in comparison with the ground truth (Table 4.10).

TABLE 4.10. Pipeline segmentation results

	U-Net		U-Net + Snake	
Slice	**Dice LV/Err LV**	**Dice MYO/Err MYO**	**Dice LV/Err LV**	**Dice MYO/Err MYO**
Basal	0.9364 / 0.03804	0.9533 / 0.8427	0.9344 / -0.2319	0.9365 / -0.2858
Mid	0.9612 / -0.2132	0.9845 / 0.4779	0.9589 / -0.4472	0.9769 / -0.4379
Apical	0.7069 / 0.2242	0.8590 / 0.7535	0.7048 / 0.3056	0.8544 / 0.8002

Upon a comprehensive evaluation of the results, it becomes apparent that, much like the active contour segmentation approach, the nnU-Net model also encounters challenges when it comes to segmenting smaller structures, notably the LV in the apical slices. The LV structure, being highly irregular and relatively small during the ED phase, presents significant complexity for accurate segmentation.

However, while the application of active contours does not lead to a substantial increase in accuracy, it merely marginally reduces the Dice score by up to 0.0168. This reduction is within an acceptable range, especially when considering the trade-off of achieving smoother structures that are conducive to feature extraction.

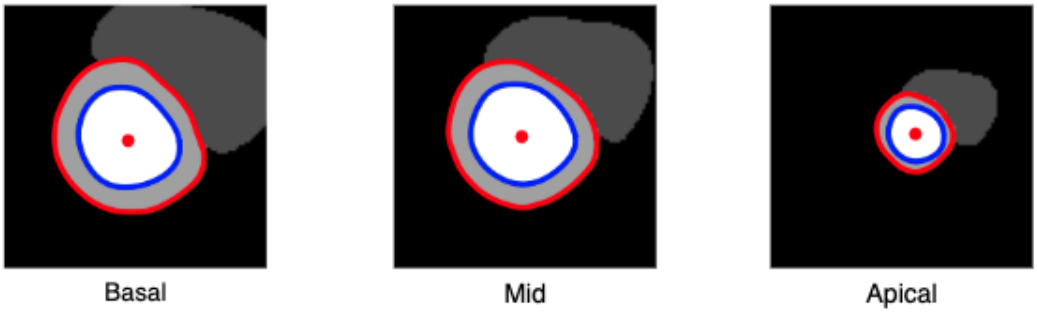

FIGURE 4.4. Boundary Enhancement Result.

CHAPTER 5

Feature Extraction

In the preceding chapter, a segmentation layer was defined. The primary objective of this layer was not to enhance the Dice score of the final segmentation but rather to focus on refining the surface of the initial segmentation produced by the pre-trained nnU-Net. We aimed to achieve smoother structures, all while ensuring that the overall accuracy loss remained minimal. These efforts were made with the goal of having well-defined structures that can enhance the feature extraction process.

In this chapter, we present the last stage of the automatic pipeline, where the goal shifts into the calculation of relevant features for cardiac disease diagnosis. In it, we explore the definition of points of interest to explore local features across the cardiac cycle, and the calculation of local and global features that aim to aid in the diagnosis of cardiac conditions. The features provided by this stage of the pipeline are also validated through the Affidea Caselas dataset.

5.1. Feature Selection

In cardiac MRI analysis, several global and local features are assessed to evaluate the structure and function of the heart. It is relevant to acknowledge that the selection of features to assess in this study is contingent upon the clinical inquiry and the unique conditions of the patients involved. Consequently, in this section, we present both local and global features for analysis in the proposed pipeline:

Global Features

- **Left Ventricular Ejection Fraction** (LVEF): LVEF is a crucial parameter that measures the percentage of blood pumped out of the left ventricle within the cardiac cycle. It provides important information about the heart's pumping function and is a key indicator of overall cardiac health;
- **Ventricular Volume**: These measurements help assess the overall size and function of the ventricle and can be used to monitor changes over time.

Local Features

- **Myocardial Wall Thickness**: Measuring the thickness of the myocardial walls, is critical not only in assessing the general health of the heart but in identifying regions where the issue resides. This feature is used to assess conditions such as hypertrophic cardiomyopathy;
- **Myocardial Wall Thickening**: The thickening of the myocardial walls, gives a representation of a segment's contractile function throughout the whole cardiac cycle, being also very relevant in the assessment of conditions;

- **Center Distance** is a measure that presents distance from specific points on both the Left Ventricle (LV) and Myocardium (MYO) contours to its center of mass, also providing insights into the spatial dynamics of the heart's contractile function.

5.2. Implementation

Local features are extracted at every frame of the cardiac cycle to provide direct information on the LV and MYO behavior during both systole and diastole. To assess some of these features, in this section, we present a point pairing method to enable the definition of segments within the MYO, which allows for thickness to be calculated throughout the structure. Furthermore, the definition of these point pairs also allows for center distance to be calculated from both the MYO and the LV boundaries. Unlike local features, global features do not require the output of the boundary enhancement stage to yield results. Instead, in this section, we propose for these features an approach that will intake the base segmentation returned by the nnU-Net and assess it in its entirety.

5.2.1. Point Pairing Method For Local Feature Asessment

The pipeline provides the possibility of defining several interest points across the LV contour that will be used for feature extraction. It is important to note that this specified number of points should not exceed the predetermined LV point limits for each specific segmentation, which are 50 points for apical slices and 100 points for mid and basal slices. Furthermore, it is pertinent to highlight that the measurement intervals between these points of interest will not be expressed in pixels or millimeters. Instead, the intervals will be represented as the distance between one point of interest and the subsequent one.

This distinction is particularly significant because contracted areas within the structure are likely to exhibit higher point densities, resulting in a non-uniform distribution. This approach aims to capture the inherent variations in the myocardial wall thickness more accurately, ultimately enhancing the precision of our measurements. It is outside the scope of the study to find the optimal number of interest points, instead, the platform aims to provide a solution that is flexible enough to adapt to different numbers of points, considering different use cases.

For correctly assessing local features, especially MYO thickness it is critical that a pairing method is defined to connect the LV and MYO boundaries, depicted in Figures 5.1 and 5.2. Once the points of interest within the LV contour have been identified (P1), it is necessary to establish their corresponding pairs in the outer MYO contour (P2). This pairing is crucial for accurately calculating myocardial thickness and other local features. Below we present the extraction process of this point pairing method, done in three stages:

(1) **Tangent Calculation**: To find the tangent at an interesting point (P1) in the LV contour, we calculate the slope of the line tangent to the contour at that specific point. This tangent line represents the direction of the LV border at that point during the cardiac cycle.

(2) **Perpendicular Line**: Next, we construct a perpendicular line that emanates from the interest point within the LV contour. This perpendicular line is oriented orthogonally to the tangent line and extends outward.

(3) **Intersection with MYO Contour**: The point where the perpendicular line intersects with the MYO contour (P2) is designated as the pair point of interest. Note that the perpendicular line will intersect the contour on both sides, to pick the actual pair, we calculate the Euclidean distance of both intersections, to the origin point, and pick the closest.

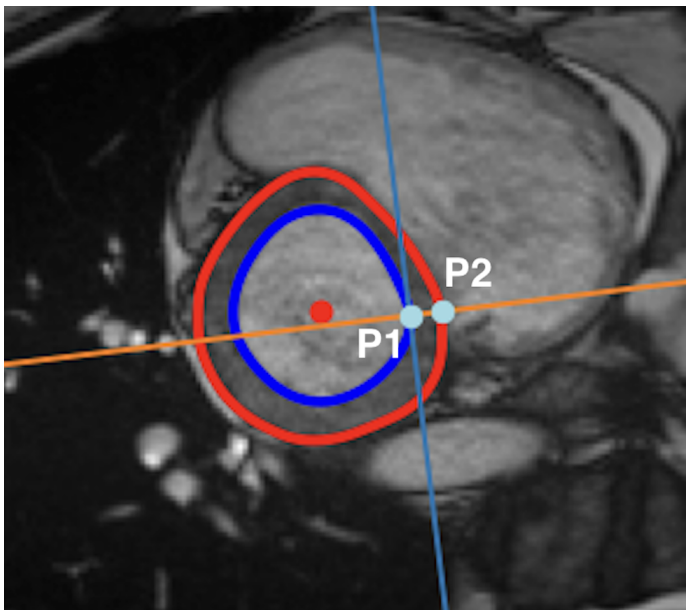

FIGURE 5.1. Point Pairing Method.

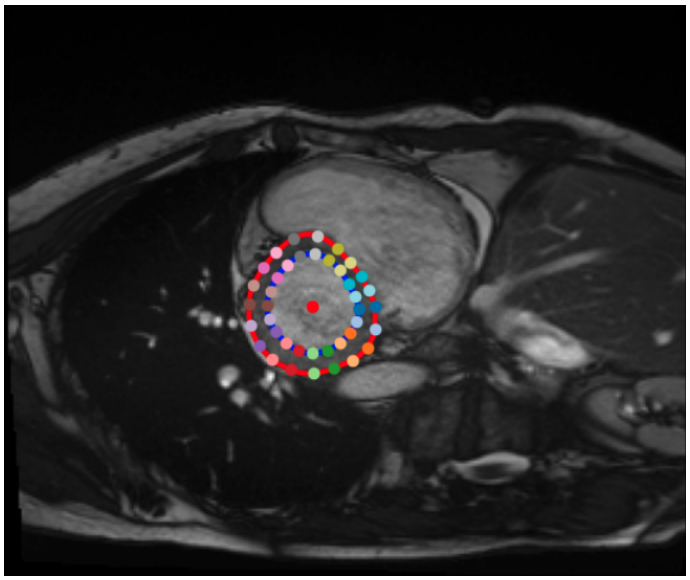

FIGURE 5.2. Point pairing method output for 20 interest points.

In summary, this approach ensures the accurate determination of LV points to their MYO contour counterparts, facilitating reliable measurements of local features throughout the cardiac cycle.

5.2.2. Thickness

Thickness is calculated through the Euclidean distance between designated LV points of interest and their corresponding counterparts within the MYO contour, as mentioned above (P1 and P2). This calculation leverages the active contour's intrinsic ability to track motion, ensuring that the interest points remain within a comfortable range from one frame to the next. The spatial information thus captured is recorded for each set of points.

$$distance = \sqrt{(x_2 - x_1)^2 + (y_2 - y_1)^2} \tag{5.1}$$

5.2.3. Thickening

Thickening is calculated by comparing the thickness of the myocardial walls at two critical points in the cardiac cycle: End of Diastole (ED) and End of Systole (ES). This measurement captures the change in wall thickness between these two phases, providing essential information about the heart's contractility. Based on the previous calculation of thickness for each frame, and set of points, we can assess the thickening of each pair through the following equation:

$$thickening = \frac{\text{ED\_thickness - ES\_thickness}}{\text{ED\_thickness}} \tag{5.2}$$

5.2.4. Center Distance

Much like thickness, center distance is determined through the application of Euclidean distance calculations, but with a different focus. This metric assesses the distance between individual contour points and the center of mass of the LV and can be calculated for both MYO and LV contours separately. This calculation offers a comprehensive view of the spatial dynamics of both structures, by assessing the range of motion for each contour point.

5.2.5. Volume and Ejection Fraction

As the literature presents, one of the most common techniques for left-ventricular volume assessment is the use of Simpson's rule. Which involves calculating the left-ventricular area of each short-axis slice and multiplying it by its thickness [**57**]. This was therefore the technique of choice for this calculation.

$$ejectionfraction = \frac{EDV - ESV}{EDV} \times 100\% \tag{5.3}$$

5.2.6. Geometry Libraries

Our local feature extraction process relies on trigonometry and geometric operations to measure spatial relations between structures (LV and MYO). For the execution of these operations, two libraries were chosen to create, manipulate, and analyze shapes: Shapely

and Sympy.

Shapely

An open-source Python package with a BSD license, purpose-built for the manipulation and analysis of planar geometric objects. It leverages the robust GEOS library, which is widely used as the engine behind PostGIS and is a port of Java Topology Suite. Shapely serves as a wrapper around GEOS, offering a versatile Geometry interface for individual geometric shapes and, at the same time, high-performance NumPy ufuncs for conducting operations on arrays of geometries.

While Shapely doesn't primarily focus on data serialization formats or coordinate systems, it is designed to seamlessly integrate with packages that do, making it a valuable tool for a wide range of applications involving geometric data.

The library provides a number of geometric objects and operations that allow the creation, manipulation, and derivation of shapes, as well as tools for spatial analysis and comparison of structures, namely Linear Rings for the objective of this research. Linear Rings are well-defined geometric constructs in the context of spatial analysis. They represent a closed loop of coordinates, which is a natural way to describe the boundaries of regions like the LV and MYO. By converting the segmentation output into these objects, we are adopting a standard geometric representation that simplifies further processing.

SymPy

Also, a BSD-licensed library is a lightweight alternative for symbolic mathematics and aims to be a full-featured computer algebra system. Given its versatility and lightweight it is mostly used in this context to define tangents and perpendiculars to more complex structures, defined in Shapely objects.

For all geometric operations in this chapter, points, tangents, and perpendiculars were defined with SymPy while intersections and the active contours were defined with shapely structures. All structures are therefore normalized in geometric objects pertaining to one of these libraries.

5.3. Results and Validation

To our current knowledge, no public dataset provides medically labeled data over features such as thickness, making an assessment of accuracy for the proposed feature extraction methods impossible at this stage. Regardless, there are standard values presented in the literature, for healthy patients. There is also a label for healthy patients in both datasets used in our work. Therefore a first validation will focus on identifying if the produced values from our pipeline accurately follow the standard values for a healthy group of patients within the private dataset. Furthermore, this section explores the explainability of specific conditions with the extracted features from the pipeline in comparison to standard values.

5.3.1. Ejection Fraction

This validation work aims to find that healthy patients yield standard values for the features extracted by the pipeline. Furthermore, the opposite is also analyzed as diagnosed patients should yield values also consistent with their condition. Starting by analyzing ejection fraction and volumes for the Affidea Caselas dataset population, the pipeline returned the results presented in Table 5.2.

TABLE 5.1. Standard LV EF and volume-related Features [**65**]

	Mean ($\pm SD$)	**Male**	**Female**	**p value**
LV Ejection Fraction (%)	69 ± 6	69 ± 6	69 ± 6	.80
LV End-Diastolic Volume (mL)	150 ± 31	160 ± 29	135 ± 26	$< .001$
LV End-Systolic Volume (mL)	47 ± 15	50 ± 16	42 ± 12	$< .001$

TABLE 5.2. Ejection fraction and volume per patient group

Patient Group	**Ejection Fraction (%)**	**End Diastolic (ml)**	**End Systolic (ml)**
Healthy_Patients	55.33% ± 5.34	131.35 ± 26.22	58.02 ± 9.87
DCM_Patients	36.81% ± 10.42	212.12 ± 47.92	134.55 ± 41.50
HCM_Patients	61.91% ± 12.61	138.36 ± 56.77	58.86 ± 41.13

As seen in the above table, healthy patients have presented values of ejection fraction of 55.33% in average with a 5.34 standard deviation. According to the literature [**65**] we can validate that these values are within the standard for a healthy heart. The literature also validates that ED and ES phase volumes are within the standard range for healthy patients. In comparison, a closer look at Dilated Cardiomyopathy (DCM) classified patients, presents an average ejection fraction below 40% which can be considered within the risk zone for cardiac failure [**66**]. In what concerns volumes, DCM patients show an above-average volume for both ED and ES stages in comparison to healthy patients, further proving that the pipeline consistently identifies issues within the ill cardiac examples. Finally, for Hypertrophic Cardiomyopathy (HCM) patients ejection fractions presented are within standard levels with ED and ES volumes very similar to those presented by healthy patients.

5.3.2. Wall Thickness

For a more detailed assessment, a look at local features will further prove the value of the pipeline in the diagnosis of left ventricular conditions. With the goal of providing concise data, the minimum and maximum thicknesses of the MYO were recorded with the goal of identifying if the range of values is also within the standard defined in the literature for healthy patients [**67**]. In Tables 5.3 and 5.4 we present standard thickness values for healthy patients in apical, basal, and mid slices.

By evaluating the results yielded from the proposed pipeline, for healthy subjects, we can assess that Basal and Mid slices provided values within the average defined in the

Table 5.3. Standard left ventricular myocardial thickness (LVMT) - Women [**67**]

Segment	**LVMTmin±SD**	**LVMTmax±SD**
Basal Slices	4.9 ±0.8	7.8 ±1.4
Mid-Cavity Level	4.1 ±0.8	6.8 ±1.4
Apical Slices	4.1 ±0.9	8.1 ±1.4

Table 5.4. Standard left ventricular myocardial thickness (LVMT) - Men [**67**]

Segment	**LVMTmin±SD**	**LVMTmax±SD**
Basal Slices	4.9 ±0.8	7.8 ±1.4
Mid-Cavity Level	4.1 ±0.8	6.8 ±1.4
Apical Slices	4.1 ±0.9	8.1 ±1.4

Table 5.5. Left ventricular myocardial thickness (LVMT) - Healthy

Segment	**LVMTmin±SD (mm)**	**LVMTmax±SD (mm)**	**Thickening**
Basal Slices	4.13 ± 1.26	7.91 ± 0.96	48.52 %
Mid-Cavity Level	4.90 ± 0.47	9.32 ± 0.94	47.12 %
Apical Slices	3.60 ± 0.46	6.32 ± 0.81	40.54 %

literature, for both the LVMTmin and LVMTmax. However, apical slices present lower average thickness values, yielding 3.60 mm ± 0.46 and 6.32 mm ± 0.81, for LVMTmin and LVMTmax, respectively, falling slightly below standard values. As argued in Chapter 4, apical slices are those in which the segmentation process is more challenging, yielding less accurate results, which can be an indicator as to why these values are below expectation.

Table 5.6. Left ventricular myocardial thickness (LVMT) - HCM

Segment	**LVMTmin±SD (mm)**	**LVMTmax±SD (mm)**	**Thickening**
Basal Slices	4.12 ± 1.01	7.33 ± 1.43	43.68 %
Mid-Cavity Level	8.36 ± 1.20	14.55 ± 1.38	42.42 %
Apical Slices	5.13 ± 0.98	7.80 ± 1.26	35.04 %

Furthermore, a closer inspection of thickness within HCM patients distinctly shows that the average max thickness widely exceeds normal values defined for healthy patients, providing an indicator that can aid in disease diagnosis. In contrast, DCM is not a condition that can be assessed solely with thickness evaluation, as it presents cases in which the left ventricular cavity expands. Usually, the contractile functionality decreases, resulting in lower EF, as described previously.

Table 5.7. Left ventricular myocardial thickness (LVMT) - DCM

Segment	**LVMTmin±SD (mm)**	**LVMTmax±SD (mm)**	**Thickening**
Basal Slices	4.92 ± 1.47	9.42 ± 1.64	53.28 %
Mid-Cavity Level	4.22 ± 0.75	7.36 ± 1.48	40.13 %
Apical Slices	3.35 ± 0.83	5.10 ± 1.22	33.15 %

5.3.3. Center Distance

Center distance, while not commonly employed in clinical studies for comparative validation, remains an integral feature subject to visual assessment by medical practitioners as a means of quantifying contractile functionality.

TABLE 5.8. Center distance (mm) measurements - Healthy

Segment	**CDmin±SD (mm)**	**CDmax±SD (mm)**	**Variation**
Basal Slices	24.78 ± 1.75	34.87 ± 1.45	28.58 %
Mid-Cavity Level	22.57 ± 1.35	33.32 ± 1.44	32.42 %
Apical Slices	9.07 ± 0.52	17.70 ± 0.65	49.94 %

TABLE 5.9. Center distance (mm) measurements - HCM

Segment	**CDmin±SD (mm)**	**CDmax±SD (mm)**	**Variation**
Basal Slices	22.09 ± 1.92	33.37 ± 1.96	33.90 %
Mid-Cavity Level	17.26 ± 1.05	31.12 ± 1.77	47.07 %
Apical Slices	8.41 ± 0.61	16.40 ± 1.26	51.30 %

TABLE 5.10. Center distance (mm) measurements - DCM

Segment	**CDmin±SD (mm)**	**CDmax±SD (mm)**	**Variation**
Basal Slices	31.59 ± 1.84	41.43 ± 1.47	23.74 %
Mid-Cavity Level	29.82 ± 1.78	38.36 ± 1.71	24.42 %
Apical Slices	12.77 ± 0.83	18.81 ± 0.87	33.40 %

Upon closer inspection, DCM subjects yielded distinctly high values of CDmin and CDmax, in comparison to healthy and HCM patients. Center distance variation also yielded results below healthy and HCM subjects. These values are consistent with the knowledge that DCM subjects are prone to have a more expanded LV cavity and less contractile functionality.

CHAPTER 6

Conclusions

In this section we go through the last remarks and conclusions, providing results and addressing the research questions explored throughout the work. Moreover, we propose areas for future work, identifying potential avenues for further research and development, considering areas of improvement, and envisioning how this work can be used as a foundation for future advancements.

6.1. Conclusion

Through this work, we proposed a fully automatic pipeline that improves state-of-the-art segmentation methods to extract features critical for left ventricular (LV) functionality evaluation. First, we used a pre-trained nnU-Net, a Fully Convolutional Neural Network (FCN) capable of segmenting an entire cardiac cycle. This first segmentation approach achieved dice scores of 0.94 (Basal), 9.96 (Mid), and 0.7 (Apical) for LV segmentation, and 0.95 (Basal), 0.98 (Mid), 0.86(Apical) for Myocardium (MYO) segmentation, on the ACDC test set. These results have shown that current state-of-the-art methods can be leveraged as a reliable basis for function assessment, although there are some areas of improvement namely the apical slice segmentation. Subsequently, two active contours were applied to enhance boundary definition while maintaining the nnU-Net's degree of accuracy. In the same test set the nnU-Net in combination with active contours yielded 0.93 (Basal), 0.96 (Mid), and 0.7(Apical) for LV segmentation and 0.94 (Basal), 0.98(Mid), and 0.85(Apical) for MYO segmentation. This enhancement not only allows for more reliable feature analysis, by providing smoother contours closer to those of anatomical structures but also reduces the possibility of anatomically impossible segmentations.

In the scope of this dissertation, a new private dataset was constructed and used to further validate the pipeline against unknown data. With this data, our proposed automatic model for feature extraction was tested and compared to clinical standards. The proposed point-pairing method allowed for accurate segment identification and measurements within the MYO and LV, at a low computational cost, in comparison to PDE approaches presented in the literature. Through this method, all local features were assessed. Thickness and thickening proved consistent for healthy patients with standard values presented in the literature. Global features, namely ejection fraction and volumes, were calculated through Simpson's rule, also presenting values within the standard range for healthy patients. Through local and global features, a clear deviation from standard

values could be found for both Hypertrophic Cardiomyopathy (HCM) and Dilated Cardiomyopathy (DCM), further showing that the pipeline adapts well to different conditions and may be able to aid in diagnosis by presenting clinically relevant data.

6.2. Future Work

One of the central challenges in medical imaging and cardiac analysis, which future work should address, is the lack of large datasets. Current available data is of small dimensions which can account for some of the issues seen in current deep learning approaches. Although remarkable accomplishments have been achieved in the area of medical image segmentation, even state-of-the-art segmentation methods such as the one used in this work, can still produce anatomically impossible segmentation in some instances (in this case disregarded by the automatic pipeline). Furthermore both extremities of the LV structure present challenges to segmentation methods. In the base of the ventricle due to valves appearing in some frames of the image, and in the apical end due to the reduced size of the object of the segmentation. The use of larger datasets would provide a more comprehensive representation of the inherent variability in medical images. This exposure to diverse cases, pathologies, and image acquisition conditions could help deep learning methods achieve better results in unseen data, improving performance on a wider range of cases.

The data issue is also transversal to the feature extraction efforts. Current datasets fail to provide extensive labeling of local features throughout the cardiac cycle, making it difficult to evaluate the accuracy of the feature extraction methods. The creation of a dataset curated with this type of information would be valuable to make a qualitative comparison between the proposed approaches.

Focussing on the current edge cases that are more prone to failure by the current segmentation approaches (basal and apical slices) some measures should be explored with the objective of improving accuracy. Some solutions worth exploring would be improvements in pre-processing measures and providing higher quality and more identifiable structures. Spatial context integration, the process of incorporating contextual information from neighboring slices also seems promising work that could yield improved results in these edge cases.

Finally, leveraging the proposed work for classification purposes to identify potential illnesses and regions of illness within the cardiac structure is also worth exploring in future research.

Bibliography

[1] World Health Organization, "Cardiovascular diseases." https://www.who.int/health-topics/cardiovascular-diseases. Accessed: 2023-10-20.

[2] R. J. van der Geest and J. H. Reiber, "Quantification in cardiac mri," *Journal of Magnetic Resonance Imaging: An Official Journal of the International Society for Magnetic Resonance in Medicine*, vol. 10, no. 5, pp. 602–608, 1999.

[3] M. R. Kaus, J. Berg, J. Weese, W. Niessen, and V. Pekar, "LV Segmentation Challenge Motivation," *IEEE Trans Image Process Med. Image Anal*, vol. 9, no. 83, pp. 1238–1248, 2000.

[4] C. Petitjean, M. A. Zuluaga, W. Bai, J. N. Dacher, Grosgeorge, *et al.*, "Right ventricle segmentation from cardiac MRI: A collation study," *Medical Image Analysis*, vol. 19, no. 1, pp. 187–202, 2015.

[5] A. Suinesiaputra, B. R. Cowan, J. P. Finn, C. G. Fonseca, A. H. Kadish, D. C. Lee, P. Medrano-Gracia, S. K. Warfield, W. Tao, and A. A. Young, "Left Ventricular Segmentation Challenge from Cardiac MRI: A Collation Study," in *Statistical Atlases and Computational Models of the Heart. Imaging and Modelling Challenges* (O. Camara, E. Konukoglu, M. Pop, K. Rhode, M. Sermesant, and A. Young, eds.), (Berlin, Heidelberg), pp. 88–97, Springer Berlin Heidelberg, 2012.

[6] "The 2015 kaggle second annual data science bowl.." https://www.kaggle.com/c/second-annual-data-science-bowl/overview/description. Accessed: 2021-07-01.

[7] O. Bernard, A. Lalande, C. Zotti, F. Cervenansky, X. Yang, *et al.*, "Deep Learning Techniques for Automatic MRI Cardiac Multi-Structures Segmentation and Diagnosis: Is the Problem Solved?," *IEEE Transactions on Medical Imaging*, vol. 37, no. 11, pp. 2514–2525, 2018.

[8] G. J. Tortora and B. Derrickson, *Principles of Anatomy and Physiology*. John Wiley & Sons, 2017.

[9] C. Clinic, "Heart chambers." https://my.clevelandclinic.org/health/body/23074-heart-chambers. Accessed: 2023-10-20.

[10] I. Kim and G. Hong, "Intraventricular flow: More than pretty pictures," *Heart Fail Clin*, vol. 15, pp. 257–265, April 2019.

[11] J. Koschate, U. Drescher, A. Werner, L. Thieschäfer, and U. Hoffmann, "Cardiovascular regulation: associations between exercise and head-up tilt," *Can J Physiol Pharmacol*, vol. 97, pp. 738–745, August 2019.

[12] M. D. Cerqueira, N. J. Weissman, V. Dilsizian, A. K. Jacobs, S. Kaul, W. K. Laskey, D. J. Pennell, J. A. Rumberger, T. Ryan, and M. S. Verani, "Standardized myocardial segmentation and nomenclature for tomographic imaging of the heart," *A Statement for Healthcare Professionals From the Cardiac Imaging Committee of the Council on Clinical Cardiology of the American Heart Association*, 2002.

[13] P. P. Sengupta, B. K. Khandheria, J. Korinek, J. Wang, A. Jahangir, J. B. Seward, and M. Belohlavek, "Apex-to-base dispersion in regional timing of left ventricular shortening and lengthening," *Journal of the American College of Cardiology*, vol. 47, no. 1, pp. 163–172, 2006.

[14] P. Chapman, J. Clinton, R. Kerber, T. Khabaza, T. Reinartz, C. Shearer, R. Wirth, *et al.*, "Crisp-dm 1.0: Step-by-step data mining guide," *SPSS inc*, vol. 9, no. 13, pp. 1–73, 2000.

[15] F. Isensee, P. F. Jaeger, P. M. Full, I. Wolf, S. Engelhardt, and K. H. Maier-Hein, "Automatic cardiac disease assessment on cine-mri via time-series segmentation and domain specific features," in *Statistical Atlases and Computational Models of the Heart. ACDC and MMWHS Challenges: 8th*

International Workshop, STACOM 2017, Held in Conjunction with MICCAI 2017, Quebec City, Canada, September 10-14, 2017, Revised Selected Papers 8, pp. 120–129, Springer, 2018.

[16] C. Petitjean and J. N. Dacher, "A review of segmentation methods in short axis cardiac MR images," *Medical Image Analysis*, vol. 15, no. 2, pp. 169–184, 2011.

[17] M. H. Hesamian, W. Jia, X. He, and P. Kennedy, "Deep Learning Techniques for Medical Image Segmentation: Achievements and Challenges," *Journal of Digital Imaging*, vol. 32, no. 4, pp. 582–596, 2019.

[18] J. Long, E. Shelhamer, and T. Darrell, "Fully convolutional networks for semantic segmentation," in *Proceedings of the IEEE conference on computer vision and pattern recognition*, pp. 3431–3440, 2015.

[19] O. Ronneberger, P. Fischer, and T. Brox, "U-net: Convolutional networks for biomedical image segmentation," in *Medical Image Computing and Computer-Assisted Intervention–MICCAI 2015: 18th International Conference, Munich, Germany, October 5-9, 2015, Proceedings, Part III 18*, pp. 234–241, Springer, 2015.

[20] M. R. Avendi, A. Kheradvar, and H. Jafarkhani, "A combined deep-learning and deformable-model approach to fully automatic segmentation of the left ventricle in cardiac MRI," *Medical Image Analysis*, vol. 30, pp. 108–119, 2016.

[21] S. Queirós, D. Barbosa, B. Heyde, P. Morais, J. L. Vilaça, D. Friboulet, O. Bernard, and J. D'hooge, "Fast automatic myocardial segmentation in 4D cine CMR datasets," *Medical Image Analysis*, vol. 18, no. 7, pp. 1115–1131, 2014.

[22] H. Hu, Z. Gao, L. Liu, H. Liu, J. Gao, S. Xu, W. Li, and L. Huang, "Automatic segmentation of the left ventricle in cardiac MRI using local binary fitting model and dynamic programming techniques," *PLoS ONE*, vol. 9, no. 12, pp. 1–17, 2014.

[23] P. V. Tran, "A fully convolutional neural network for cardiac segmentation in short-axis mri," *arXiv preprint arXiv:1604.00494*, 2016.

[24] T. A. Ngo and G. Carneiro, "Fully automated non-rigid segmentation with distance regularized level set evolution initialized and constrained by deep-structured inference," in *2014 IEEE Conference on Computer Vision and Pattern Recognition*, pp. 3118–3125, 2014.

[25] S. Warfield, K. Zou, and W. Wells, "Simultaneous truth and performance level estimation (staple): An algorithm for the validation of image segmentation," *IEEE transactions on medical imaging*, vol. 23, pp. 903–21, 08 2004.

[26] B. Li, Y. Liu, C. J. Occleshaw, B. R. Cowan, and A. A. Young, "In-line Automated Tracking for Ventricular Function With Magnetic Resonance Imaging," *JACC: Cardiovascular Imaging*, vol. 3, no. 8, pp. 860–866, 2010.

[27] M.-P. Jolly, C. Guetter, X. Lu, H. Xue, and J. Guehring, "Automatic Segmentation of the Myocardium in Cine MR Images Using Deformable Registration," in *Statistical Atlases and Computational Models of the Heart. Imaging and Modelling Challenges* (O. Camara, E. Konukoglu, M. Pop, K. Rhode, M. Sermesant, and A. Young, eds.), (Berlin, Heidelberg), pp. 98–108, Springer Berlin Heidelberg, 2012.

[28] J. Margeta, E. Geremia, A. Criminisi, and N. Ayache, "Layered Spatio-temporal Forests for Left Ventricle Segmentation from 4D Cardiac MRI Data," in *Statistical Atlases and Computational Models of the Heart. Imaging and Modelling Challenges* (O. Camara, E. Konukoglu, M. Pop, K. Rhode, M. Sermesant, and A. Young, eds.), (Berlin, Heidelberg), pp. 109–119, Springer Berlin Heidelberg, 2012.

[29] M. A. Zuluaga, M. J. Cardoso, M. Modat, and S. Ourselin, "Multi-atlas Propagation Whole Heart Segmentation from MRI and CTA Using a Local Normalised Correlation Coefficient Criterion,"

in *Functional Imaging and Modeling of the Heart* (S. Ourselin, D. Rueckert, and N. Smith, eds.), (Berlin, Heidelberg), pp. 174–181, Springer Berlin Heidelberg, 2013.

[30] C.-W. Wang, C.-W. Peng, and H.-C. Chen, "A simple and fully automatic right ventricle segmentation method for 4-dimensional cardiac mr images," *Proceedings of MICCAI RV segmentation challenge*, 2012.

[31] J. Long, E. Shelhamer, and T. Darrell, "Fully convolutional networks for semantic segmentation," in *Proceedings of the IEEE conference on computer vision and pattern recognition*, pp. 3431–3440, 2015.

[32] C. F. Baumgartner, L. M. Koch, M. Pollefeys, and E. Konukoglu, "An exploration of 2d and 3d deep learning techniques for cardiac mr image segmentation," in *Statistical Atlases and Computational Models of the Heart. ACDC and MMWHS Challenges: 8th International Workshop, STACOM 2017, Held in Conjunction with MICCAI 2017, Quebec City, Canada, September 10-14, 2017, Revised Selected Papers 8*, pp. 111–119, Springer, 2018.

[33] Y. Jang, Y. Hong, S. Ha, S. Kim, and H.-J. Chang, "Automatic Segmentation of LV and RV in Cardiac MRI," in *Statistical Atlases and Computational Models of the Heart. ACDC and MMWHS Challenges* (M. Pop, M. Sermesant, P.-M. Jodoin, A. Lalande, X. Zhuang, G. Yang, A. Young, and O. Bernard, eds.), (Cham), pp. 161–169, Springer International Publishing, 2018.

[34] C. Zotti, Z. Luo, O. Humbert, A. Lalande, and P.-M. Jodoin, "Gridnet with automatic shape prior registration for automatic mri cardiac segmentation," in *Statistical Atlases and Computational Models of the Heart. ACDC and MMWHS Challenges: 8th International Workshop, STACOM 2017, Held in Conjunction with MICCAI 2017, Quebec City, Canada, September 10-14, 2017, Revised Selected Papers 8*, pp. 73–81, Springer, 2018.

[35] M. Khened, V. Alex, and G. Krishnamurthi, "Densely Connected Fully Convolutional Network for Short-Axis Cardiac Cine MR Image Segmentation and Heart Diagnosis Using Random Forest," in *Statistical Atlases and Computational Models of the Heart. ACDC and MMWHS Challenges* (M. Pop, M. Sermesant, P.-M. Jodoin, A. Lalande, X. Zhuang, G. Yang, A. Young, and O. Bernard, eds.), (Cham), pp. 140–151, Springer International Publishing, 2018.

[36] J. M. Wolterink, T. Leiner, M. A. Viergever, and I. Išgum, "Automatic segmentation and disease classification using cardiac cine mr images," in *Statistical Atlases and Computational Models of the Heart. ACDC and MMWHS Challenges: 8th International Workshop, STACOM 2017, Held in Conjunction with MICCAI 2017, Quebec City, Canada, September 10-14, 2017, Revised Selected Papers 8*, pp. 101–110, Springer, 2018.

[37] J. Patravali, S. Jain, and S. Chilamkurthy, "2d-3d fully convolutional neural networks for cardiac mr segmentation," in *Statistical Atlases and Computational Models of the Heart. ACDC and MMWHS Challenges: 8th International Workshop, STACOM 2017, Held in Conjunction with MICCAI 2017, Quebec City, Canada, September 10-14, 2017, Revised Selected Papers 8*, pp. 130–139, Springer, 2018.

[38] M.-M. Rohé, M. Sermesant, and X. Pennec, "Automatic multi-atlas segmentation of myocardium with svf-net," in *Statistical Atlases and Computational Models of the Heart. ACDC and MMWHS Challenges: 8th International Workshop, STACOM 2017, Held in Conjunction with MICCAI 2017, Quebec City, Canada, September 10-14, 2017, Revised Selected Papers 8*, pp. 170–177, Springer, 2018.

[39] G. Tziritas, "Fully-automatic segmentation of cardiac images using 3-d mrf model optimization and substructures tracking," in *Reconstruction, Segmentation, and Analysis of Medical Images: First International Workshops, RAMBO 2016 and HVSMR 2016, Held in Conjunction with MICCAI 2016, Athens, Greece, October 17, 2016, Revised Selected Papers 1*, pp. 129–136, Springer, 2017.

[40] X. Yang, C. Bian, L. Yu, D. Ni, and P.-A. Heng, "Class-balanced deep neural network for automatic ventricular structure segmentation," in *Statistical Atlases and Computational Models of the Heart. ACDC and MMWHS Challenges: 8th International Workshop, STACOM 2017, Held in Conjunction with MICCAI 2017, Quebec City, Canada, September 10-14, 2017, Revised Selected Papers 8*, pp. 152–160, Springer, 2018.

[41] F. Isensee, P. F. Jäger, S. A. Kohl, J. Petersen, and K. H. Maier-Hein, "Automated design of deep learning methods for biomedical image segmentation," *arXiv preprint arXiv:1904.08128*, 2019.

[42] G. M. Beache, V. J. Wedeen, and R. E. Dinsmore, "Magnetic resonance imaging evaluation of left ventricular dimensions and function and pericardial and myocardial disease," *Coronary Artery Disease*, vol. 4, no. 4, pp. 328–333, 1993.

[43] I. Olivotto, R. Gistri, P. Petrone, E. Pedemonte, D. Vargiu, and F. Cecchi, "Maximum left ventricular thickness and risk of sudden death in patients with hypertrophic cardiomyopathy," *Journal of the American College of Cardiology*, vol. 41, no. 2, pp. 315–321, 2003.

[44] O. Turschner, J. D'hooge, C. Dommke, P. Claus, E. Verbeken, I. D. Scheerder, B. Bijnens, and G. R. Sutherland, "The sequential changes in myocardial thickness and thickening which occur during acute transmural infarction, infarct reperfusion and the resultant expression of reperfusion injury," *European Heart Journal*, vol. 25, pp. 794–803, May 2004.

[45] R. J. van der Geest, A. de Roos, E. E. van der Wall, and J. H. Reiber, "Quantitative analysis of cardiovascular mr images," *The International Journal of Cardiac Imaging*, vol. 13, pp. 247–258, 1997.

[46] N. Beohar, J. D. Flaherty, C. J. Davidson, M. I. Vidovich, A. Brodsky, D. C. Lee, E. Wu, E. L. Bolson, R. O. Bonow, and F. H. Sheehan, "Quantitative assessment of regional left ventricular function with cardiac mri: three-dimensional center-surface method," *Catheterization and Cardiovascular Interventions*, vol. 69, no. 5, pp. 721–728, 2007.

[47] W. Xue, I. B. Nachum, S. Pandey, J. Warrington, S. Leung, and S. Li, "Direct estimation of regional wall thicknesses via residual recurrent neural network," in *Information Processing in Medical Imaging: 25th International Conference, IPMI 2017, Boone, NC, USA, June 25-30, 2017, Proceedings 25*, pp. 505–516, Springer, 2017.

[48] W. Xue, G. Brahm, S. Pandey, S. Leung, and S. Li, "Full left ventricle quantification via deep multitask relationships learning," *Medical image analysis*, vol. 43, pp. 54–65, 2018.

[49] A. F. Frangi, W. J. Niessen, and M. A. Viergever, "Three-dimensional modeling for functional analysis of cardiac images, a review," *IEEE transactions on medical imaging*, vol. 20, no. 1, pp. 2–5, 2001.

[50] J.-T. Hsieh, S. Zhao, S. Eismann, L. Mirabella, and S. Ermon, "Learning neural pde solvers with convergence guarantees," *arXiv preprint arXiv:1906.01200*, 2019.

[51] F. Khalifa, G. M. Beache, G. Gimelrfarb, G. A. Giridharan, and A. El-Baz, "Accurate automatic analysis of cardiac cine images," *IEEE Transactions on Biomedical Engineering*, vol. 59, no. 2, pp. 445–455, 2011.

[52] F. Van Rugge, E. Holman, E. Van der Wall, A. De Roos, A. Van der Laarse, and A. Bruschke, "Quantitation of global and regional left ventricular function by cine magnetic resonance imaging during dobutamine stress in normal human subjects," *European heart journal*, vol. 14, no. 4, pp. 456–463, 1993.

[53] N. Reichek, "Mri myocardial tagging," *Journal of Magnetic Resonance Imaging*, vol. 10, pp. 609–616, 1999.

[54] M. Prasad, A. Ramesh, P. Kavanagh, J. Gerlach, G. Germano, D. S. Berman, and P. J. Slomka, "Myocardial wall thickening from gated magnetic resonance images using laplace's equation," in *Medical Imaging 2009: Computer-Aided Diagnosis*, vol. 7260, pp. 708–715, SPIE, 2009.

[55] Q. Huang, E. Z. Chen, H. Yu, Y. Guo, T. Chen, D. Metaxas, and S. Sun, "Measure anatomical thickness from cardiac mri with deep neural networks," in *Statistical Atlases and Computational Models of the Heart. M&Ms and EMIDEC Challenges: 11th International Workshop, STACOM 2020, Held in Conjunction with MICCAI 2020, Lima, Peru, October 4, 2020, Revised Selected Papers 11*, pp. 44–55, Springer, 2021.

[56] U. Sechtem, B. A. Sommerhoff, W. Markiewicz, R. D. White, M. D. Cheitlin, and C. B. Higgins, "Regional left ventricular wall thickening by magnetic resonance imaging: Evaluation in normal persons and patients with global and regional dysfunction," *The American Journal of Cardiology*, vol. 59, no. 1, pp. 145–151, 1987.

[57] D. Longmore, R. Klipstein, S. Underwood, and et al., "Dimensional accuracy of magnetic resonance in studies of the heart," *Lancet*, vol. 1, no. 8442, pp. 1360–1362, 1985.

[58] G. Cranney, C. Lotan, L. Dean, and et al., "Left ventricular volume measurement using cardiac axis nuclear magnetic resonance imaging: validation by calibrated ventricular angiography," *Circulation*, vol. 82, pp. 154–163, 1990.

[59] M. Lawson, G. Blackwell, N. Davis, and et al., "Accuracy of biplane long-axis left ventricular volume determined by cine magnetic resonance imaging in patients with regional and global dysfunction," *The American Journal of Cardiology*, vol. 77, pp. 1098–1104, 1996.

[60] C. W. Yancy, M. Jessup, B. Bozkurt, *et al.*, "2013 accf/aha guideline for the management of heart failure," *Journal of the American College of Cardiology*, vol. 62, pp. e147–e239, 2013.

[61] R. G. Weintraub, C. Semsarian, and P. Macdonald, "Dilated cardiomyopathy," *The Lancet*, vol. 390, no. 10092, pp. 400–414, 2017.

[62] "Nifti - neuroimaging informatics technology initiative." https://nifti.nimh.nih.gov/. Accessed: 2023-10-20.

[63] "Dicom standard." https://www.dicomstandard.org/. Accessed: 2023-10-20.

[64] B. Whitcher, V. J. Schmid, and A. Thorton, "Working with the dicom and nifti data standards in r," *Journal of Statistical Software*, vol. 44, pp. 1–29, 2011.

[65] L. E. Hudsmith, S. E. Petersen, J. M. Francis, M. D. Robson, and S. Neubauer, "Normal human left and right ventricular and left atrial dimensions using steady state free precession magnetic resonance imaging," *Journal of Cardiovascular Magnetic Resonance*, vol. 7, no. 5, p. 775–782, 2005.

[66] S. D. Solomon, N. Anavekar, H. Skali, J. J. McMurray, K. Swedberg, S. Yusuf, C. B. Granger, E. L. Michelson, D. Wang, S. Pocock, and M. A. Pfeffer, "Influence of ejection fraction on cardiovascular outcomes in a broad spectrum of heart failure patients," *Circulation*, vol. 112, no. 24, pp. 3738–3744, 2005.

[67] N. Kawel, E. B. Turkbey, J. J. Carr, J. Eng, A. S. Gomes, W. G. Hundley, and R. J. ... van der Geest, "Normal left ventricular myocardial thickness for middle-aged and older subjects with steady-state free precession cardiac magnetic resonance: The multi-ethnic study of atherosclerosis," *Circulation: Cardiovascular Imaging*, vol. 5, no. 4, p. 500–508, 2012.